

Blending data and physics for reduced-order modeling of systems  
with spatiotemporal chaotic dynamics

Alex Guo<sup>1</sup> and Michael D. Graham<sup>1</sup>

<sup>1</sup>*Department of Chemical and Biological Engineering,  
University of Wisconsin-Madison, Madison WI 53706, USA*

(Dated: July 30, 2025)

## Abstract

While data-driven techniques are powerful tools for reduced-order modeling of systems with chaotic dynamics, great potential remains for leveraging known physics (i.e. a full-order model (FOM)) to improve predictive capability. We develop a hybrid reduced order model (ROM), informed by both data and FOM, for evolving spatiotemporal chaotic dynamics on an invariant manifold whose coordinates are found using an autoencoder. This approach projects the vector field of the FOM onto the invariant manifold; then, this physics-derived vector field is either corrected using dynamic data, or used as a Bayesian prior that is updated with data. In both cases, the neural ordinary differential equation approach is used. We consider simulated data from the Kuramoto–Sivashinsky and complex Ginzburg–Landau equations. Relative to the data-only approach, for scenarios of abundant data, scarce data, and even an incorrect FOM (i.e. erroneous parameter values), the hybrid approach yields substantially improved time-series predictions.

## I. INTRODUCTION

The ability to efficiently and accurately forecast complex systems is highly sought after in engineering applications. Sometimes we know the physics (i.e. we have an exact “full-order model” (FOM)) of these systems and can perform simulations by discretizing and solving the governing equations. However, directly solving the FOM can be computationally prohibitive for systems exhibiting multiscale, spatiotemporal chaos, especially when many solutions must be found, as is typical for tasks such as design and control. Here, we are interested in developing high-fidelity, computationally efficient reduced-order models (ROMs) of the long-time dynamics of systems with complex spatiotemporal chaotic behavior. In this work, we combine data-driven methods with a physics-based FOM method to develop a hybrid ROM for forecasting spatiotemporally chaotic systems, demonstrating that even an approximate FOM can substantially enhance predictive performance relative to an approach using only data.

Perhaps the simplest approach for hybrid data-physics ROMs for systems governed by partial differential equations, is the “proper orthogonal decomposition (POD)-Galerkin” method [1]. POD, also known as principal component analysis (PCA), uses data to discover an orthogonal basis ordered by variance (energy in the case of fluid flow): I.e. the first basis vector

points in the direction of maximal variance in the data set, and so on. In POD-Galerkin, the governing equations are projected onto a subset of the POD basis, yielding evolution equations for the POD amplitudes. This approach has been applied to the Navier-Stokes equations in an effort to develop low-dimensional models of turbulent flows [1–3]. A significant limitation of POD-Galerkin is that it implicitly takes the data to lie on a linear subspace of the full state space (i.e. a flat manifold), which is not generally a good assumption, and may lead to a very large number of POD modes being required to yield good performance.

Nevertheless, while data from a high-dimensional system such as the Navier-Stokes Equations (NSE) may not lie in a linear subspace, because of energy dissipation, it is expected at long times to lie on a finite-dimensional invariant manifold [4, 5]. For finding a nonlinear coordinate transformation to an invariant manifold, one can use an undercomplete autoencoder (AE) [6, 7]. An AE uses a feedforward neural network to map data from the state space to a low-dimensional latent space, and another neural network for the reverse mapping. AEs have been used to reduce dimension in turbulent flows [8–10] and other chaotic partial differential equation (PDE) systems [11, 12]. For the second step of learning the dynamics on the manifold coordinates, one can use the neural ordinary differential equations (NODEs) [13] method. Using the time-dependent data, a NODE learns the vector field (RHS) of the dynamical system governing the data as a neural network. The latent space coordinates found using an AE can also be forecasted with recurrent neural networks (RNNs), as demonstrated in [14, 15]); more general approaches for reduced-order, dynamical modeling can be found in [16–18]. We denote the approach of using a NODE to time-evolve the low-dimensional latent space given by an AE as “data-driven manifold dynamics” (DManD) [19]. Altogether, DManD is a purely data-driven ROM. DManD has been previously used for reduced-order modeling of several chaotic dynamical systems [20–29]. Incorporating symmetries in DManD substantially aids in training efficiency and predictive performance [30–32]. Linot and Graham [33] found that with fewer than 20 degrees of freedom, a DManD model of weakly turbulent plane Couette flow quantitatively captured key features of the flow that required 1000 degrees of freedom in a POD-Galerkin approach, despite the DManD approach having no information about the underlying governing equations. The present work illustrates how to augment DManD with a FOM.

Dimension reduction aside, a widely used method for combining physics and machine

learning for learning solutions to PDEs is physics-informed neural networks (PINNs) [34, 35]. PINNs use a physics-based loss term that penalizes the residual of the PDE at collocation points to learn PDE solutions that are physically consistent. While PINNs may also include a supervised loss on the initial and boundary conditions from data measurements, the solution is mostly influenced by the purely physics-based loss — therefore, PINNs are often regarded as ODE or PDE solvers that are not data-driven. Nonetheless, the use of a PINN-like loss term in data-driven frameworks is quite common. One example is in physics-informed deep learning [36], where the data-driven loss is placed on points outside of the initial and boundary conditions. In [37, 38], a PINN-like loss term is used with neural operators [39, 40], which are data-driven techniques for learning PDE solution operators. For the most part, PINNs are not designed to produce accurate solutions outside the time horizon of the collocation points used in training, though some work [41] has been done to address this issue. By contrast, predicting forward in time over an arbitrarily long horizon is the central topic of the present work. Because PINNs are not necessarily data-driven, not reduced-order, and not designed for time-series prediction, we do not consider this approach further.

We now arrive at the physics-based method on which our hybrid ROM described later is based. This method is called Manifold Galerkin (MG) [12]. MG is an accurate FOM-based method that nonlinearly projects the governing equations onto a manifold learned from data in the form of an autoencoder. That is, Manifold Galerkin is similar to POD-Galerkin, just with a nonlinear rather than linear coordinate transformation to a lower-dimensional manifold. Although the MG model provides the vector field in a reduced-dimensional space (which can then be time-integrated for trajectory predictions), it is often more expensive to integrate than the FOM because the vector field must still be evaluated in the original high-dimensional state space at each time step. The authors of [12] suggest hyper-reduction approaches (i.e. reducing the mesh size on which the FOM is evaluated) to address this problem of MG, which has been demonstrated in [42]. MG will be discussed in more detail in Section II.

To the best of our knowledge, [43] is the only work besides ours that uses MG as a physics-based method to inform a data-driven forecasting model. In that work, the authors developed a hybrid physics-informed NODE (PINODE) method, which applies a soft constraint to the vector field on an autoencoder latent space learned by a NODE; this soft constraint drives the

RHS learned by the NODE to the RHS of the MG model, where the former is more efficient to integrate than the latter. Our hybrid ROM (described next) differs from the PINODE method [43] in a few key ways, which are described in Section V C. We make a notable mention to the hybrid method in [44], where the FOM (subject to some approximation error) is directly combined with a reservoir computing network to forecast the state space of a chaotic system; however, since reservoir networks have a hidden state with dimensionality higher than the original state space, this hybrid method is not a ROM. Additionally, reservoir networks are inherently non-Markovian techniques (which is also true for RNNs [45, 46] and transformers [9, 47, 48]) that use past history information to make time series predictions. For data that comes from a memoryless dynamical system such as differential equation, these approaches do not maintain this dynamical systems structure. Our aim is to develop reduced-order models that maintain a differential equation structure.

In this paper, we combine the purely data-driven approach DManD with the physics-based MG method to develop a hybrid ROM framework that we call physics-informed DManD (PI-DManD). We briefly describe the workflow for our hybrid ROM in Section II, with a more detailed exposition in Section V. In Section III, we apply the approach to the prediction of spatiotemporal chaos in the Kuramoto–Sivashinsky equation when varying the amount of training data and the accuracy of the physics-based prior information provided by MG. The Supplementary Information includes results for the complex Ginzburg–Landau equation (CGLE) [49, 50], another system exhibiting spatiotemporal chaos. In all cases, PI-DManD leads to substantial improvements in predictive capability.

## II. WORKFLOW

### A. Setup

We work with state space data  $u \in \mathbb{R}^{d_u}$ , where  $d_u$  is the state space dimension, sampled with uniform data spacing  $\tau$ . Given time series data of  $u$  generated from a PDE or experiments, we aim to develop a ROM that can be used for time evolution predictions. The time

series data come from the underlying (ground truth) autonomous dynamical system

$$\frac{du}{dt} = f(u; \mu), \quad (1)$$

where  $f$  is the true vector field that depends on physical parameters  $\mu$  (e.g. domain length). Unless the data are from simulations,  $f$  and  $\mu$  are generally not known. Still, one often has some knowledge or model of the underlying physics. Assume that we know a full-order model (FOM) of the true dynamical system in Equation 1, written as

$$\frac{du}{dt} = f_{\text{FOM}}(u; \mu_{\text{FOM}}), \quad (2)$$

where  $f_{\text{FOM}}$  is the vector field for the model and  $\mu_{\text{FOM}}$  are the physical parameters of the FOM. The field  $f_{\text{FOM}}$  may only be approximate due to the lack of full first-principles knowledge of the system, while  $\mu_{\text{FOM}}$  may only be approximate if the data are from experiments and there is uncertainty in the parameters.

## B. DManD

As discussed in Section I, the first step in building a ROM with the present approach is to use an undercomplete autoencoder (AE) [51] to find a low-dimensional, high-fidelity latent representation of  $u$ . An AE consists of two parts. The encoder  $\mathcal{E}$  nonlinearly maps  $u$  to the latent space  $h \in \mathbb{R}^{d_h}$ , where  $d_h < d_u$ . The decoder  $\mathcal{D}$  performs the reverse mapping  $\tilde{u} = \mathcal{D}(h) = \mathcal{D}(\mathcal{E}(u))$ , where  $\tilde{u}$  is the reconstruction. Ideally,  $d_h$  will equal the embedding dimension of the invariant manifold containing the time series data. Further discussion of this point is found in Supplementary Section S1C1.

With the AE in hand, the DManD approach to reduced-order modeling learns a dynamical system in the latent space:

$$\frac{dh}{dt} = g(h), \quad (3)$$

where  $g$  is the true vector field in the manifold coordinates. We use the NODE method [52] to approximate the vector field  $g$  as a neural network  $g_d$ . A schematic of DManD is depicted in Figure 1(a) and (b). See Section VA for details on DManD.

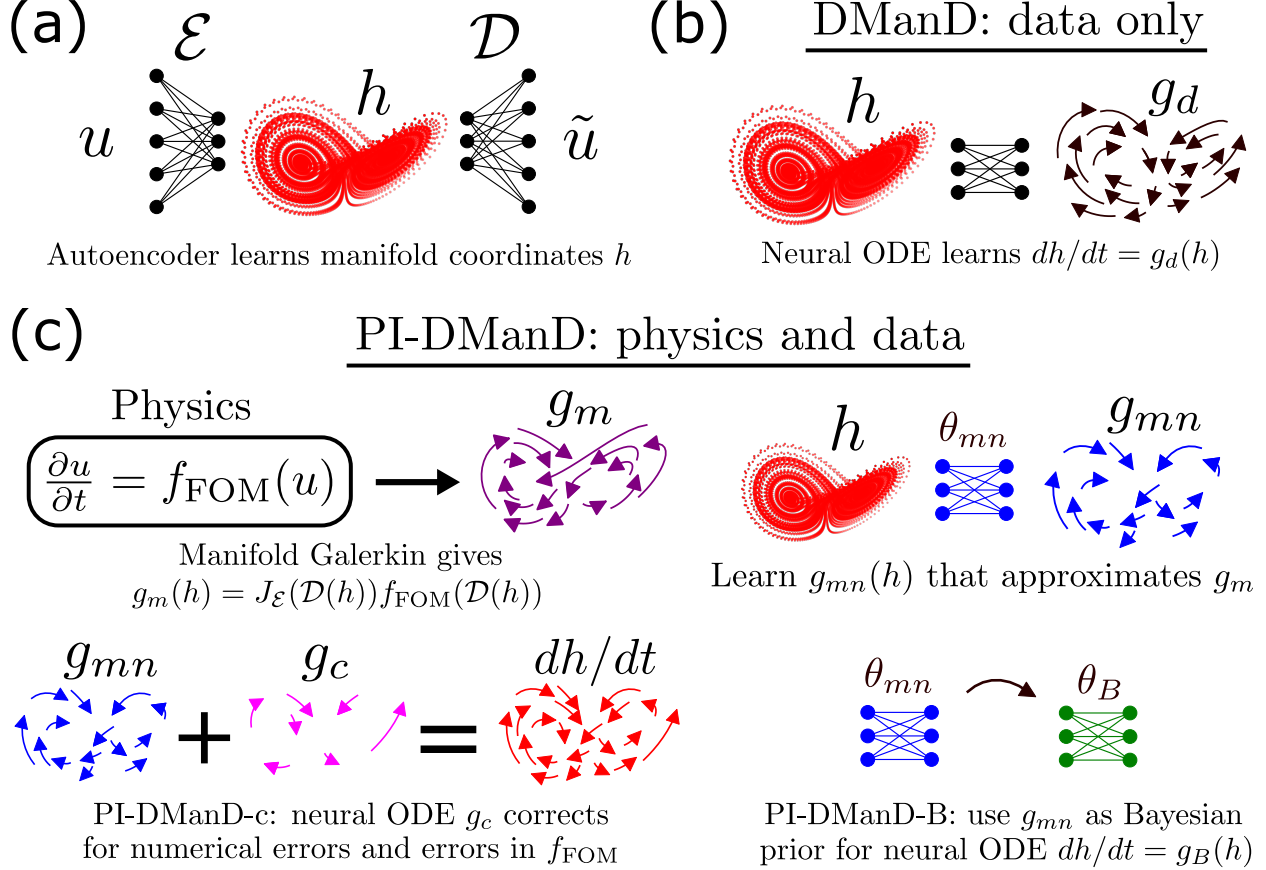


**FIG. 1:** Data-driven manifold dynamics (DManD) is a data-driven ROM that reduces dimension of the state  $u$  with an autoencoder (a) and evolves trajectories with a vector field on the latent space  $h$  learned by a neural ODE (b). (c) Physics-informed DManD (PI-DManD) is a hybrid ROM that uses Manifold Galerkin to project the vector field on the full order model (FOM)  $f_{\text{FOM}}$  onto that of the latent space, learns a neural network approximation of the latent space vector field as  $g_{mn}$ , and either uses a corrective neural ODE  $g_c$  to fix numerical and FOM approximation errors (PI-DManD-c) or uses  $g_{mn}$  as a Bayesian prior for training a DManD model (PI-DManD-B).

### C. PI-DManD

We provide a brief overview of incorporating physics into DManD to create two separate physics-informed DManD (PI-DManD) methods (see Section V for details). Both PI-DManD methods are based on a physics-informed ROM, where the two steps of forming it are illustrated in the top row of Figure 1(c). First, we use MG to find the vector field of the FOM on the latent space:  $g_m = \frac{\partial \mathcal{E}(u)}{\partial u} f_{\text{FOM}}(\mathcal{D}(h))$ . Then, we use a neural network to approximate  $g_m$  as  $g_{mn}$ , thus avoiding the computational inefficiency of MG. We call this resulting physics-informed ROM ‘‘MG-neural network (MG-N)’’.

PI-DManD arises from combining MG-N with DManD. We do this in two ways, which are illustrated in the bottom row of Figure 1(c). The first method simply uses the NODE approach to find a neural network  $g_c$  such that  $g_{mn} + g_c \approx g$ ; i.e.  $g_c$  is an additive data-driven correction term to the MG-N vector field. We call this method “PI-DManD-c”. The second method can be viewed as a Bayesian or transfer learning approach, which we call “PI-DManD-B”. PI-DManD-B finds, again with the NODE method, a vector field  $g_B \approx g$  whose weights  $\theta_B$  are initialized as the MG-N network weights  $\theta_{mn}$  and whose loss includes a weight-decay-like term that drives the weights of  $g_B$  toward those of the MG-N prior. Both PI-DManD methods use data to correct for numerical and FOM approximation errors. The last type of error is inherent in the MG-N method when  $f_{\text{FOM}} \neq f$  and/or  $\mu_{\text{FOM}} \neq \mu$ .

### III. RESULTS

We work with data generated from the Kuramoto–Sivashinsky equation (KSE), which is a 1D PDE exhibiting spatiotemporal chaos [19, 44, 53] and is widely used as a test bed for data-driven methods. The KSE is given by

$$\frac{\partial u}{\partial t} = -u \frac{\partial u}{\partial x} - \frac{\partial^2 u}{\partial x^2} - \frac{\partial^4 u}{\partial x^4}. \quad (4)$$

We use a domain length of  $L = 22$  with periodic boundary conditions, wherein the solution exhibits chaotic dynamics and has a Lyapunov time  $\tau_L$  of 22.2 time units [54, 55]. For this KSE system, the dimension of the invariant manifold is empirically known to be  $d_M = 8$  [19, 54, 56, 57]; therefore, we will use  $d_h = 8$  as the dimension for the AE. We generate a long trajectory using an exponential time-differencing RK4 (ETD-RK4) solver [58] in the Fourier domain. We remove the transient and use  $M = 500,000$  snapshots of  $u$  discretized on  $d_u = 64$  uniformly spaced grid points, separated by  $\tau = 0.25$  time units. We use the first 80% of the dataset for training, so that the number of training snapshots  $N$  is 400,000. The last 100,000 snapshots are for testing (even when we do not use the whole training dataset, as in Section III B). See Section V D for other training details.

We test whether the hybrid ROMs (PI-DManD-c and PI-DManD-B) can outperform the DManD ROM, which is solely data-driven. In Section III A, we train the methods using the whole time series. In Section III B, we consider three subcases of using a subset of the

time series (note, for one subcase, we will generate and use a new time series dataset with  $N = 400,000$  and  $\tau > 0.25$ ). In Section [III C](#), we consider the case when the parameters used in the FOM do not match the simulation parameters used to generate the data — this models the situation when the FOM is not exact. (In Supplementary Section [S1 C](#), we repeat the tests reported here for the 1D CGLE.)

### A. Abundant data, exact FOM

Here, we use the entire training dataset and the exact physics ( $f_{\text{FOM}} = f$ ) for the MG/MG-N methods. We gauge model performance on how well the model predictions (latent space trajectories that have been decoded back to the full space) track the true solution over a time horizon of  $3\tau_L$  — any good method should be able to make reasonably accurate predictions over at least  $\tau_L$ . We calculate the ensemble-averaged, normalized tracking error

$$\epsilon(t) = \left\langle \frac{\|u(t) - \hat{u}(t)\|_2}{\|u(t)\|_2} \right\rangle, \quad (5)$$

where  $\hat{u}(t)$  is the model prediction trajectory, and the ensemble average  $\langle \cdot \rangle$  is calculated using 300 non-overlapping trajectories whose initial conditions are from the testing dataset. In Figure [2\(a\)](#), we plot the tracking error  $\epsilon(t)$  for DManD, the physics-informed methods (MG and MG-N), and the two hybrid methods. Here, all non-DManD methods perform similarly and display much smaller error than DManD — at  $t = \tau_L$ , their error is smaller by a factor of two; this result suggests that including physics aids in model predictions when the provided physics are exact. Figure [2\(b\)](#) shows space-time plots of representative trajectories for ground truth and the DManD and PI-DManD-c model predictions. The differences between the ground truth and model trajectories in Figure [2\(b\)](#) are plotted in Figure [2\(c\)](#), indicating that noticeable differences arise sooner for DManD than for PI-DManD-c. (Representative trajectories and difference plots for other models, not shown, look similar to those of PI-DManD-c due to similar error curves  $\epsilon(t)$  — see Figure [2\(a\)](#).) In this case where we have a large amount of closely spaced training data and the FOM is exact, all physics-informed and hybrid methods outperform DManD in short-time forecasting.

Figure [2\(d\)](#) shows the evolution of  $\epsilon(t = \tau_L)$  during the course of NODE training, for DManD and the two PI-DManD variants. Most notably, the correction vector field  $g_c$  learned

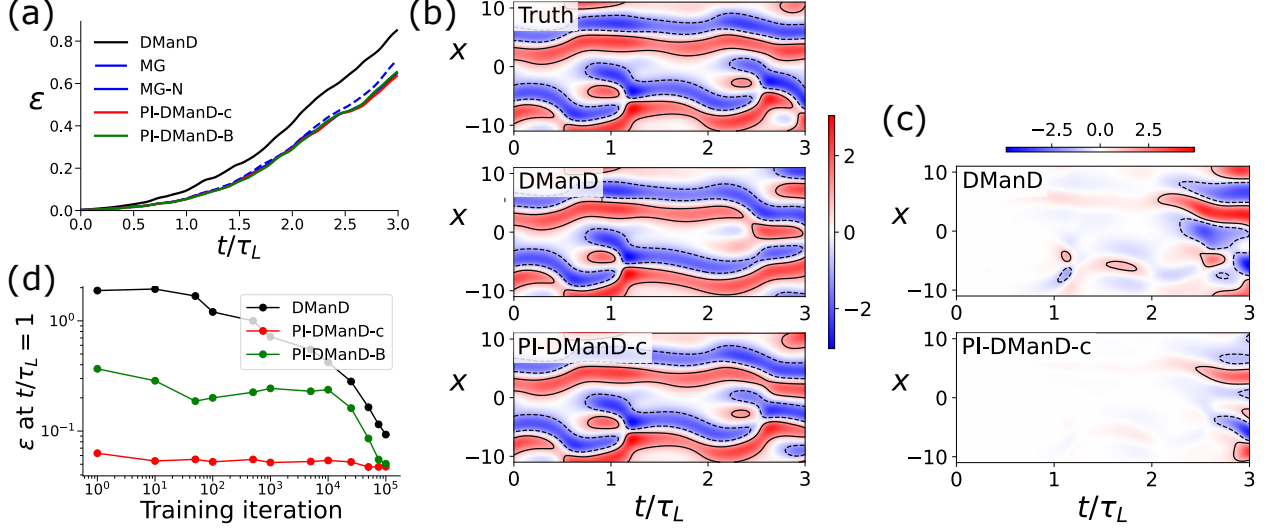


**FIG. 2:** KSE,  $L = 22$  (for both data and FOM),  $N = 400,000$ ,  $\tau = 0.25$ . (a) Ensemble-averaged short-time tracking error for all methods. (b) Representative trajectories of ground truth and model predictions (contours at  $u = \pm 1$ ). (c) Difference plots between ground truth and model predictions (contours at difference values of  $\pm 1$ ). Representative trajectories and difference plots for other models look similar to those of PI-DManD-c. (d) NODE training convergence for purely data-driven and hybrid methods.

by PI-DManD-c converges several orders of magnitude faster than the vector field  $g_d$  learned by DManD. However, since PI-DManD-c (and PI-DManD-B) are derived from MG-N, the MG-N training time to learn  $g_{mn}$  must also be accounted for — in this case, the time to just train MG-N is around 4 times longer than the time to train DManD (see details in Supplementary Section S1A). While the combined training time for PI-DManD-c is longer than for DManD, it still has the benefit of better predictive performance. As for the inference time, all models except MG perform comparably — since MG is not a ROM, it takes 9 to 48 times longer to evolve an initial condition than the other methods (see Supplementary Tables S1 and S2).

In Supplementary Section S1B, we evaluate how well the solution trajectories stay on the true attractor at long times by calculating the joint probability density function (pdf) of some key quantities. There, we show that all five methods captured this long-time statistic equally well.

## B. Scarce data, exact FOM

While still using the exact FOM, we now study the effect of having less data (training data size  $N < 400,000$ ), data spaced further apart ( $\tau > 0.25$ ), or both. We apply this data-scarce training for the AE, the MG-N network, and all NODEs. To prevent overfitting, the weight decay strength in all neural network training is increased here (see training details in Section V D).

We first fix the data spacing at  $\tau = 0.25$  and vary the training data size from  $N = 400,000$  to 100,000, 25,000, and 10,000. In other words, we use a shorter part of our time series data. Figure 3(a) shows the ensemble-averaged tracking error  $\epsilon$  at one Lyapunov time for these four values of  $N$ . Above each group of bars in Figure 3(a), we report the percent error for the AE reconstruction

$$\epsilon_{\text{AE}} = \left\langle \frac{\|u_i - \tilde{u}_i\|_2}{\|u_i\|_2} \right\rangle_i \times 100\%, \quad (6)$$

and the percent error for MG-N in approximating the MG vector field

$$\epsilon_{\text{MG-N}} = \left\langle \frac{\|g_m(h_i) - g_{mn}(h_i)\|_2}{\|g_m(h_i)\|_2} \right\rangle_i \times 100\%, \quad (7)$$

where  $\langle \cdot \rangle_i$  is an ensemble average across all snapshots (indexed by  $i$ ) in the testing dataset. The base case of  $N = 400,000$ , which corresponds to Figure 2(a), shows that DManD has higher tracking error, by a factor of two, than the other methods. Within the error bars, MG-N and the two hybrid methods perform comparably to DManD for  $N < 400,000$ . The reason that NODE test error  $\epsilon$  increases with decreasing  $N$  for all methods is due to increasing AE reconstruction error.

Next, we fix  $N = 400,000$  and increase  $\tau$  from 0.25 to 1, 5, and 10. As mentioned earlier, here we need to generate new time series data that cover a longer time interval than the originally used time series data of  $N = 400,000$  and  $\tau = 0.25$ . As seen in Figure 3(b), the AE, MG-N, and NODE tracking errors do not vary much with  $\tau$ . Across the three increased  $\tau$  values, PI-DManD-B has up to 30% lower error than DManD. Note that the missing PI-DManD-c bar in Figure 3(b), replaced by an asterisk, has an error of about unity and is omitted to improve clarity in the vertical axis (and similarly for bar plots elsewhere). Note that a spacing of  $\tau = 10$  corresponds to  $\approx 0.5$  Lyapunov times, and all approaches will

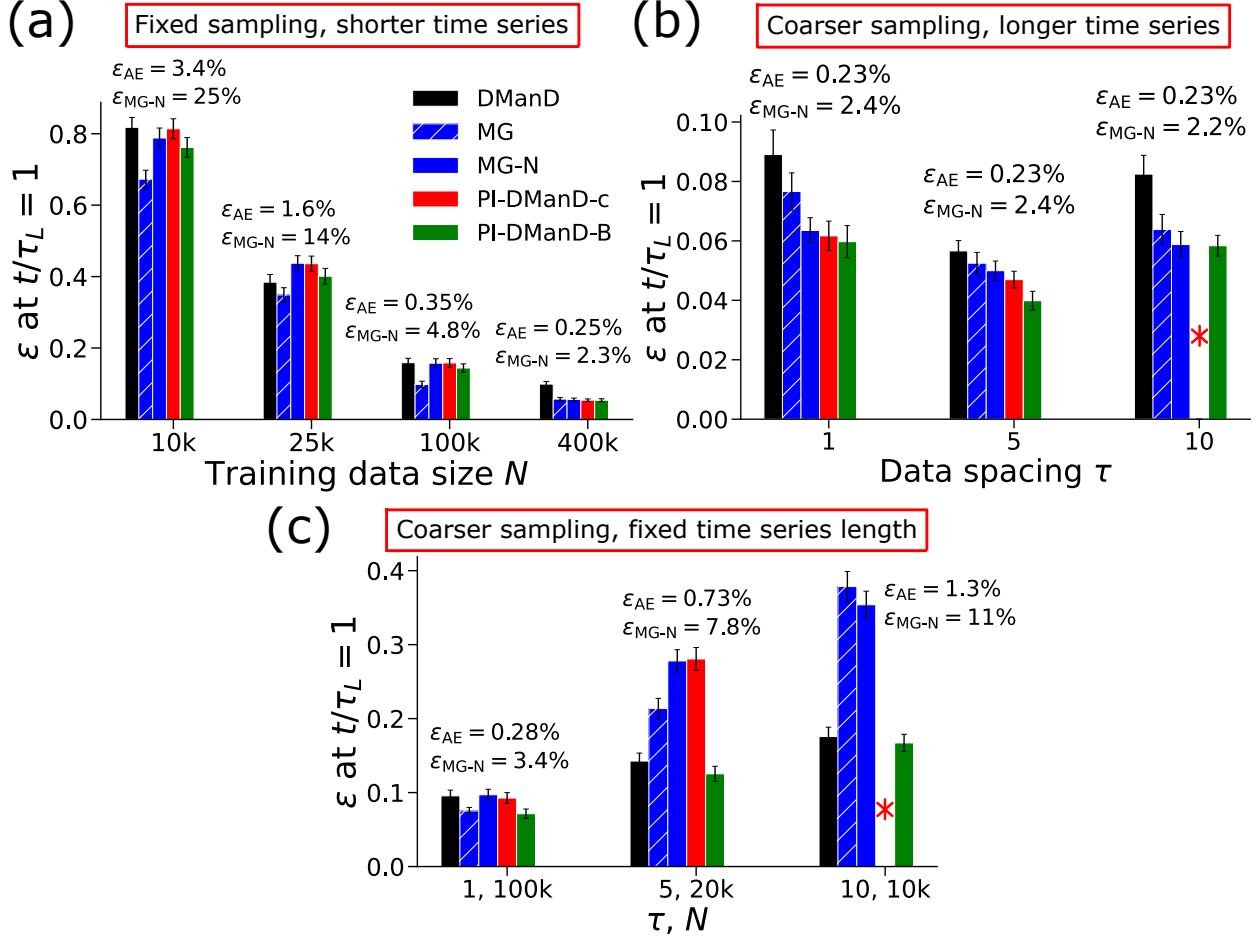


**FIG. 3:** KSE,  $L = 22$  (for both data and FOM). Short-time tracking error at one Lyapunov time for scarce data in terms of (a) less data with  $N \leq 400,000$  and  $\tau = 0.25$  (i.e. shorter time series), (b) widely spaced data with  $\tau > 0.25$  and  $N = 400,000$ , and (c) increasing  $\tau$  and decreasing  $N$  proportionally. Here and elsewhere, error bars show standard error, and all subplots follow the legend in (a). Note the different vertical axis limits for each subplot. Missing PI-DManD-c bars, denoted with asterisk, in (b) and (c) have errors of about 1 (i.e. much larger than the case shown) and are omitted to improve clarity in the vertical axis.

ultimately fail as  $\tau$  becomes comparable to the Lyapunov time; we find that PI-DManD-c fails first. Unlike the previously considered scenario with just decreasing  $N$ , here we see sizable improvements of PI-DManD-B over DManD.

In the final subcase here, we simultaneously increase  $\tau$  and decrease  $N$  by downsampling the original time series dataset ( $N = 400,000$  and  $\tau = 0.25$ ). In Figure 3(c), we show the tracking error for downsample factors of 4, 20, and 40; here, only PI-DManD-B has a tracking error that remains comparable to that of DManD (and is slightly lower in the case of  $\tau = 1$ ,  $N = 100,000$ ). Across these three subcases of data-scarce training, PI-DManD-B

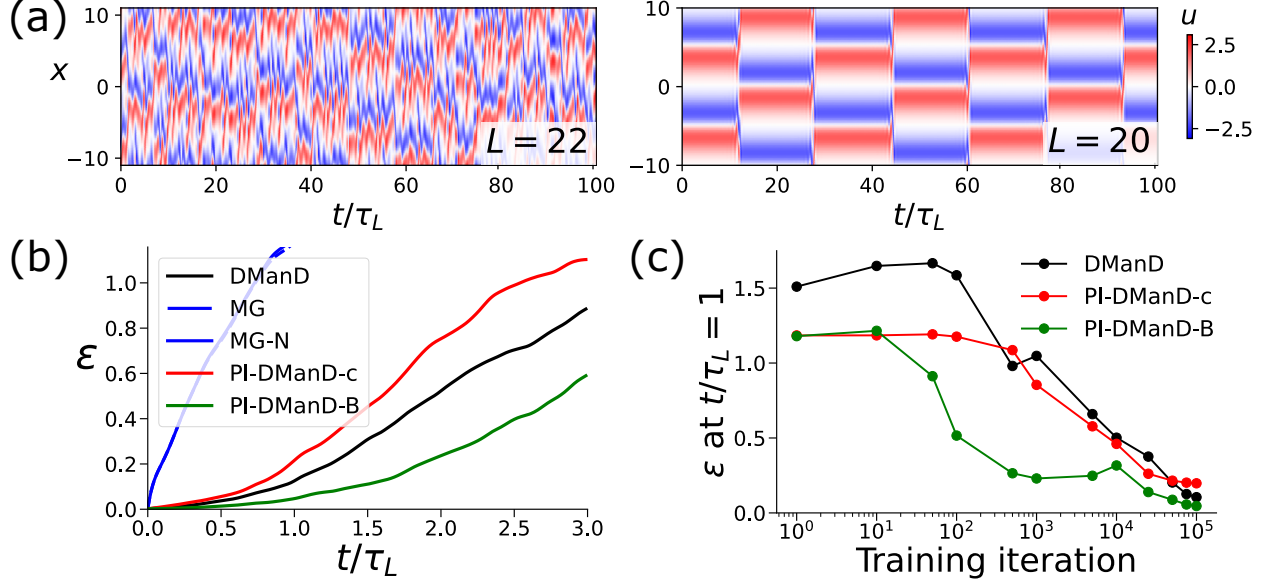


**FIG. 4:** KSE,  $N = 400,000$ ,  $\tau = 0.25$ . Effects of using an erroneous parameter ( $L = 20$ ) in the FOM to model data generated with  $L = 22$ . (a) Ground truth trajectory (left) and example trajectory with erroneous parameter (right). (b) Ensemble-averaged short-time tracking error. (c) NODE training convergence for purely data-driven and hybrid methods.

has equal or lower error than DManD while PI-DManD-c sometimes has a higher error than DManD.

### C. Erroneous FOM

An accurate FOM is not available for many physical systems, either because of a lack of first-principles knowledge of the governing equations, or uncertainty in the parameter values used in the FOM. Here we test the robustness of our hybrid methods to parameter error by purposely using an incorrect domain length  $L = 20$  in the FOM instead of the correct value of  $L = 22$  used to generate the data (i.e.  $\mu_{\text{FOM}} \neq \mu$ ). In other words, the model manifold vector field  $g_m$  is generated from  $f_{\text{FOM}}$  with incorrect parameter values. Figure 4(a) shows the space-time plots of example trajectories for  $L = 22$  and  $L = 20$ . With the smaller domain length, the dynamics display intermittent/bursting-like behavior that is very different from that found at  $L = 22$ . To be clear, we never generate data with  $L = 20$  for any training or testing of our models — we only use the  $L = 22$  dataset.

To make the comparisons in this section, we use abundant training data ( $N = 400,000$

and  $\tau = 0.25$ ). Figure 4(b) shows the tracking error for all methods. Since DManD does not use any knowledge of the FOM, its short-time tracking performance is comparable to that in Figure 2(a) (these two NODE models for DManD only differ by the random weight initialization). As expected, the solely physics-informed MG and MG-N methods have poor short-time tracking due to only trying to learn the vector field in the latent coordinates from the FOM (see Equation 13) and not from the data. Since PI-DManD-c uses data to correct for FOM errors, its tracking error is lower than that of MG-N; as shown in Figure 4(c), the NODE training convergence for  $g_c$  of PI-DManD-c converges slower as compared to the exact FOM case in Figure 2, indicating that correcting FOM errors requires more training iterations than only correcting for numerical errors. While PI-DManD-c does not outperform DManD in short-time tracking, PI-DManD-B does. This result indicates that even if the FOM of the physics-based prior is highly erroneous, the hybrid PI-DManD-B ROM can still substantially outperform the solely data-driven DManD ROM in short-time tracking. As for long-time statistics, both hybrid ROMs perform similarly to DManD (see Supplementary Section S1B).

#### IV. CONCLUSION

In this work, we found that including physics-based prior information substantially improves the predictive capabilities of data-driven ROMs applied to systems with spatiotemporal chaotic dynamics, even if the physics-based information is not completely correct. We built upon previous work on a solely data-driven ROM called DManD [19] — which uses a neural ODE (NODE) approach to learn the dynamics on an invariant manifold whose coordinates are found with an autoencoder — by incorporating ideas from the Manifold Galerkin (MG) method [12]. MG expresses the RHS of the ODE in the latent space coordinates in terms of the RHS of the FOM (i.e. the physics). We approximated the MG vector field with a neural network (which we call MG-N) and combined it with DManD to develop two hybrid ROMs. The first, which we call PI-DManD-c, adds a correction term learned by a NODE to the MG-N vector field in order to account for numerical errors and inherent errors in the FOM. The second hybrid ROM is a DManD model with an additional weight-decay-like term in the loss that drives the weights of a NODE network toward those of the MG-N

network (and a transfer learning step from the latter to the former). This second hybrid ROM can be viewed as using MG-N as a Bayesian prior for training a NODE, and we call it PI-DManD-B.

We applied DManD and our hybrid ROMs (PI-DManD-c and PI-DManD-B) to the KSE and the 1D CGLE (results for CGLE are in the Supplementary Information), which are two PDE systems with spatiotemporal chaotic dynamics. We summarize the improvement of PI-DManD-B over DManD in making short-time predictions for three case studies in Table I. The first case study is the baseline, where we use exact physics and abundant training data; there, PI-DManD-B (and PI-DManD-c) accurately tracked the true solution for substantially longer — at one Lyapunov time, the ensemble-averaged relative short-time tracking error is 0.1 for DManD and only 0.05 for the hybrid ROMs. The second case study reduced the amount of training data (for three subcases), and the third study involved providing substantially incorrect PDE parameters to the FOM used by MG/MG-N. For these last two studies, PI-DManD-B (but not PI-DManD-C) still provided sizable improvements over DManD, thus demonstrating its robustness to scarce data and FOM errors. Future directions include testing robustness of our hybrid ROMs on complex fluid and flow systems for which only approximate first-principles models are available, and extending our methods to the case where we only have partial observations.

	Exact physics, abundant data	Exact physics, scarce data	Erroneous physics, abundant data
% reduction in relative trajectory error at $t = \tau_L$	<b>46%–51%</b> (Figs. 2(a), S4(a))	<b>≈0%</b> (shorter time series, finer sampling; Figs. 3(a), S6(a)) <b>22%–62%</b> (longer time series, coarser sampling; Figs. 3(b), S6(b)) <b>6%–29%</b> (fixed time series length, coarser sampling; Figs. 3(c), S6(c))	<b>43%–64%</b> (Figs. 4(b), S7(b), S7(c))

**TABLE I:** Summary of the improvement or reduction in  $\epsilon(t = \tau_L)$  (the relative ensemble averaged short-time tracking error at one Lyapunov time) for the hybrid PI-DManD-B method over the solely data-driven DManD method; specifically, the quantities correspond to  $(\epsilon_{\text{DManD}} - \epsilon_{\text{PI-DManD-B}})/\epsilon_{\text{DManD}} \times 100\%$ . We varied the accuracy of the known physics (i.e. the full order model), the length of the time series (i.e. number of time units covered), and the sampling rate of the data.

## V. METHODS

Given a single (or ensemble of) time series of state space data generated from a PDE or experiments, we aim to develop a ROM that can be used for time evolution predictions, especially for systems with chaotic dynamics. Despite reducing the number of degrees of freedom in the system, we desire the ROM to give accurate short-time predictions and long-time predictions that stay close to the true attractor.

Recall from Section II that we work with full state space observations  $u \in \mathbb{R}^{d_u}$ , where  $d_u$  is the state space dimension. Here, we use a single long time series of  $u$  as the dataset. We denote this dataset as  $\{u_i\}_{i=1}^M$ , where  $u_i = u(t_i)$  is the snapshot of the state at time instant  $t_i$  and  $M$  is the number of snapshots. We use a uniform data spacing of  $\tau$  time units; note that the methods described here also apply if the data spacing is not constant. This dataset comes from the underlying (ground truth) dynamical system shown in Equation 1 in Section II. We often have a FOM (see Equation 2) whose vector field  $f_{\text{FOM}}$  or parameters  $\mu_{\text{FOM}}$  may only be approximate.

In Section VA, we start by describing a solely data-driven ROM. Then in Section VB, we discuss how the MG method [12] uses the FOM in Equation 2 to create a physics-based time evolution method. Lastly, we present our hybrid ROM in Section VC, which uses the MG method to incorporate physics knowledge, while also using data to correct for the FOM approximation errors that are not addressed by MG.

### A. Data-driven manifold dynamics (DManD)

We first find a low-dimensional, high-fidelity latent representation of  $u$  for which to build the ROM. To do so, we will use an undercomplete autoencoder [51] to discover a coordinate transformation to (and from) a low-dimensional latent space representation  $h \in \mathbb{R}^{d_h}$ , where  $d_h < d_u$ . As mentioned in the Introduction, dissipative systems often have long-time dynamics that lie on an invariant manifold with dimension  $d_{\mathcal{M}} \ll d_u$ . While it is generally difficult to determine  $d_{\mathcal{M}}$ , there are a variety of methods for estimating it [54, 57].

An autoencoder consists of two back-to-back neural networks. The encoder  $\mathcal{E}$  nonlinearly maps  $u_i$  to  $h_i = \mathcal{E}(u_i)$ . The decoder  $\mathcal{D}$  performs the reverse mapping  $\tilde{u}_i = \mathcal{D}(h_i)$ , where  $\tilde{u}_i$  is the reconstructed snapshot. We minimize the reconstruction error of the autoencoder (AE)

with the loss function

$$\mathcal{L}_{\text{AE}} = \langle \|u_i - \mathcal{D}(\mathcal{E}(u_i; \theta_{\mathcal{E}}); \theta_{\mathcal{D}})\|_2^2 \rangle_i, \quad (8)$$

where  $\theta_{\mathcal{E}}$  and  $\theta_{\mathcal{D}}$  are, respectively, the neural network parameters of the encoder and decoder networks and  $\langle \cdot \rangle_i$  denotes an ensemble average over a batch of training snapshots. Here, and elsewhere, we use stochastic gradient descent to minimize the loss function.

Recall from Equation 3 in Section II that  $g$  is the true vector field in the manifold coordinates. We train a neural ODE (NODE) [52] to approximate this function. Given a latent state  $h(t_i)$ , one can calculate

$$\hat{h}_{\text{DManD}}(t_i + \tau) = h(t_i) + \int_{t_i}^{t_i + \tau} g_d(h(t'); \theta_{g_d}) dt', \quad (9)$$

where  $\hat{h}_{\text{DManD}}(t_i + \tau)$  is the NODE prediction of the latent state at the next sampled time instant, and  $g_d$  is the data-driven approximation of  $g$ . We model  $g_d$  with a deep feedforward neural network and optimize its parameters  $\theta_{g_d}$  with the loss function

$$\mathcal{L}_{\text{DManD}} = \langle \|\hat{h}_{\text{DManD}}(t_i + \tau) - h(t_i + \tau)\|_2^2 \rangle_i. \quad (10)$$

Here, we only consider the reconstruction loss for an integration time horizon spanning a single data spacing interval  $\tau$ . While one could consider a multi-step loss with a longer time horizon, we find that doing so does not improve the results and just slows down training for the systems studied here. As a side note, the use of a multi-step NODE loss may be helpful in some situations, such as for time-delay embeddings of partially observed data [24]. In the results, we will increase the data spacing  $\tau$  used in the NODE training. Lastly, we note that it has been shown recently [59] that the NODE approach is equivalent to a Koopman-operator-based method called extended dynamic mode decomposition with dictionary learning (EDMD-DL) [60] with a projection step onto the state.

Overall, this combination of an AE and a NODE to build a ROM is coined data-driven manifold dynamics (DManD) [19]. As a side note, NODE models can be stabilized for long-time predictions by following [61], in which the integrand  $g_d(h; \theta_{g_d})$  in Equation 9 is modified to  $g_d(h; \theta_{g_d}) - ah$ , where  $a > 0$ . Although [61] found that adding the linear damping term  $ah$  primarily benefits the case where there is no dimension reduction (i.e. a NODE is used to

approximate  $f_{\text{FOM}}$ ), we include the damping term nonetheless when learning  $g_d$  since doing so also has no negative effects (we use  $a = 10^{-3}$  for this paper). Lastly, we note that it is possible to simultaneously learn a latent space and a NODE model; however, we find that jointly training an autoencoder and a NODE model often requires more expressive networks, leads to slower training convergence, and does not yield improved performance.

## B. Manifold Galerkin

We now present the formalism for the Manifold Galerkin (MG) method proposed in [12], which directly expresses the vector field  $f_{\text{FOM}}$  in the manifold coordinates  $h$ . Using the chain rule and substituting  $u = \mathcal{D}(h; \theta_{\mathcal{D}})$  into the FOM in Equation 2 yields

$$\frac{dh}{dt} = \frac{d\mathcal{E}(u)}{du} \frac{du}{dt} = \frac{d\mathcal{E}(u)}{du} f_{\text{FOM}}(\mathcal{D}(h; \theta_{\mathcal{D}}); \mu_{\text{FOM}}), \quad (11)$$

Let the Jacobian of the coordinate transformation between  $u$  and  $h$  be expressed as

$$\frac{\partial \mathcal{E}(u)}{\partial u} = J_{\mathcal{E}}(\mathcal{D}(h; \theta_{\mathcal{D}}); \theta_{\mathcal{E}}). \quad (12)$$

Since  $\mathcal{E}(u)$  is a neural network, automatic differentiation can be used to easily compute this. Substituting this expression for  $J_{\mathcal{E}}$  into Equation 11 yields the final equation for MG:

$$\begin{aligned} \frac{dh}{dt} &= g_m(h; \theta_{\mathcal{E}}, \theta_{\mathcal{D}}, \mu_{\text{FOM}}), \\ g_m &= J_{\mathcal{E}}(\mathcal{D}(h; \theta_{\mathcal{D}}); \theta_{\mathcal{E}}) f_{\text{FOM}}(\mathcal{D}(h; \theta_{\mathcal{D}}); \mu_{\text{FOM}}). \end{aligned} \quad (13)$$

If the equations and parameters of the FOM are exact (i.e.  $f_{\text{FOM}} = f$  and  $\mu_{\text{FOM}} = \mu$ ) and the autoencoder is exact, then  $g_m(h)$  given by MG is the true vector field on the invariant manifold, expressed in the manifold coordinates  $h$ .

Although MG in Equation 13 has the appearance of a ROM since it provides the vector field in the latent space  $h$ , it is in fact even slower to solve than the FOM. At each timestep, MG not only retains the expense of computing  $f_{\text{FOM}}$ , but must also first decode  $h$  to  $u$  and evaluate a Jacobian (which, for  $J_{\mathcal{E}}$ , involves another encoding step). Work has been done to accelerate the MG method using hyper-reduction techniques [42], which aim to perform

approximate FOM computations that are independent of the ambient dimension  $d_u$ . Overall, MG is a physics-based method (but not a ROM) that projects the physics of the FOM onto the manifold coordinates found with a data-driven autoencoder.

The run-time expense of MG can be overcome by using a neural network to learn an approximation of the function  $g_m(h)$ . Since we know the functional form of  $f_{\text{FOM}}(u)$ , we can use the data points  $u_i$  to generate  $f_{\text{FOM},i} = f_{\text{FOM}}(u_i)$ . If the data come from simulations of the FOM, then  $f_{\text{FOM},i}$  is already computed at each time step of the simulation, so we can store it instead of recomputing it. Otherwise, the step to generate  $f_{\text{FOM},i}$  from  $u_i$  for  $i = 1, \dots, N$  only needs to be performed once as a preprocessing step. We then calculate the MG output data  $g_{m,i} = J_{\mathcal{E}}(u_i)f_{\text{FOM},i}$  for all  $i$ . We denote the neural network for mapping the inputs  $h_i = \mathcal{E}(u_i)$  to the MG outputs  $g_{m,i}$  as  $g_{mn}$ , and we train it with the loss

$$\mathcal{L}_{\text{MG-N}} = \langle \|g_{mn}(h_i; \theta_{g_{mn}}) - g_{m,i}\|_2^2 \rangle_i. \quad (14)$$

Here, only the parameters  $\theta_{g_{mn}}$  are learnable (i.e.,  $g_{m,i}$  are constants and do not depend on the network parameters of the autoencoder). One can substitute  $g_m(h)$  in Equation 13 with  $g_{mn}(h)$  to get

$$\frac{dh}{dt} = g_{mn}(h; \theta_{g_{mn}}). \quad (15)$$

Since  $g_{mn}(h; \theta_{g_{mn}})$  is a neural network approximation of  $g_m(h)$ , we call this method MG - neural network (MG-N). As will be shown in Section III, the MG-N model in Equation 15 is much faster to integrate than the MG model in Equation 13. Note that the dynamic nature of the data set is not used in development of MG/MG-N, so if the FOM is inaccurate, these approaches will model an incorrect vector field on a correct set of manifold coordinates.

### C. Physics-informed data-driven manifold dynamics (PI-DManD)

Now we describe how we incorporate physics into DManD to create two physics-informed DManD (PI-DManD) methods. There are three sources of errors when using MG-N as a ROM: numerical and test error in the autoencoder that influence the training of  $g_{mn}$ , test error in  $g_{mn}(h)$  itself, and lastly, errors in the FOM. The last type of error grows as domain-based approximation of the physics  $f_{\text{FOM}}(u, \mu_{\text{FOM}})$  deviates further from the true

underlying physics  $f(u, \mu)$  of the data. FOM error can occur if  $f_{\text{FOM}} \neq f$  and/or  $\mu_{\text{FOM}} \neq \mu$ ; the latter case may occur if there is uncertainty in the physical or PDE parameters (e.g. domain length), which will often arise if the dataset comes from experiments. In our first PI-DManD approach, denoted PI-DManD-c, we account for all three types of errors by adding a correction term,  $g_c(h)$ , to the vector field from MG-N to get our final, reduced-order dynamical model in the latent coordinates:

$$\frac{dh}{dt} = g_{mn}(h; \theta_{g_{mn}}) + g_c(h; \theta_{g_c}). \quad (16)$$

We learn  $g_c(h; \theta_{g_c})$  using a NODE approach with loss

$$\mathcal{L}_{\text{PI-DManD-c}} = \langle \|\hat{h}_{\text{PI-DManD-c}}(t_i + \tau) - h(t_i + \tau)\|_2^2 \rangle_i, \quad (17)$$

where

$$\hat{h}_{\text{PI-DManD-c}}(t_i + \tau) = h(t_i) + \int_{t_i}^{t_i + \tau} [g_{mn}(h(t'); \theta_{g_{mn}}) + g_c(h(t'); \theta_{g_c})] dt'. \quad (18)$$

Here, only the weights  $\theta_{g_c}$  are trainable (the MG-N weights  $\theta_{g_{mn}}$  are kept frozen). Altogether, PI-DManD-c learns a function  $g_{mn} + g_c$  for the latent space dynamics. While MG-N is a physics-informed ROM that can be heavily biased by the FOM approximation, PI-DManD-c is a hybrid ROM that is less susceptible to this bias, as is illustrated in the results.

The second PI-DManD approach, denoted PI-DManD-B, uses the MG-N model as a prior for training the NODE model. Specifically, we aim to learn a NODE model for the RHS of

$$\frac{dh}{dt} = g_B(h; \theta_{g_B}), \quad (19)$$

with the loss

$$\mathcal{L}_{\text{PI-DManD-B}} = \langle \|\hat{h}_{\text{PI-DManD-B}}(t_i + \tau) - h(t_i + \tau)\|_2^2 \rangle_i + \lambda_B \|\theta_{g_B} - \theta_{g_{mn}}\|_2^2, \quad (20)$$

where

$$\hat{h}_{\text{PI-DManD-B}}(t_i + \tau) = h(t_i) + \int_{t_i}^{t_i + \tau} g_B(h(t'); \theta_{g_B}) dt'. \quad (21)$$

The difference here as compared to a DManD model lies in the additional regularization term

$\|\theta_{g_B} - \theta_{g_{mn}}\|_2$ , which acts to penalize deviations of the NODE weights from the MG-N weights. The prefactor  $\lambda_B$  controls the strength of the regularization. By using this regularization term, the NODE model learns the vector field from data while also being softly constrained to the physics-derived vector field from MG-N — as compared to the correction NODE used in PI-DManD-c, this NODE for  $g_B$  is more natural in learning from the data and physics simultaneously, which yields benefits as will be shown later. Another difference is that here the NODE  $g_B$  must have the same architecture as the MG-N network, which is mostly a minor restriction. In addition to the regularization term, we perform a transfer learning step of initializing the weights of  $g_B$  to those of MG-N. So, the PI-DManD-B model uses the MG-N model  $g_{mn}$  as a physics-based prior.

The loss used by PI-DManD-B can be viewed as being motivated from a Bayesian framework. To see this, consider the regression problem  $y = m(x; \theta_m)$ , where  $\theta_m$  are the model parameters. According to Bayes' theorem, we can write the posterior distribution for the parameters  $\theta_M$  given the data  $y$  as

$$p(\theta_m | y) = \frac{p(y | \theta_m) p(\theta_m)}{p(y)}. \quad (22)$$

Assuming a normal distribution for the likelihood  $p(y | \theta_m) \propto \exp(-(y - m)^2 / 2\sigma_m^2)$  as well as for the prior  $p(\theta_m) \propto \exp(-(\theta_m - \theta_p)^2 / 2\sigma_p^2)$ , maximizing the log likelihood corresponds to minimizing the loss function

$$\mathcal{L} = \frac{1}{2\sigma_m^2} \langle (y - m)^2 \rangle + \frac{1}{2\sigma_p^2} \|\theta_m - \theta_p\|_2^2. \quad (23)$$

This expression is very similar to Eq. 20, motivating the description of PI-DManD-B as a Bayesian approach.

It must be noted that PI-DManD bears similarities to the PINODE method of [43]. PI-DManD uses knowledge of the governing equations to get the physics-derived vector field on the latent space and combines that with a NODE; however, our method differs in several key ways. First, PI-DManD only requires a dataset composed of a time series of data points, while PINODE requires additional data points called “collocation points” that are user-specified. Second, in contrast to PINODE, our PI-DManD method can be non-intrusive — in the case that the training data includes time-derivative (equivalently vector field) data

(which can be easily stored when gathering simulation data), our method can be applied to different systems without any code modification. Third, if the data are from experiments, then time-derivative data need to be generated using the vector field on the full space; in this case, we front-load the FOM evaluations required by MG into a preprocessing step of the intermediate MLP network — doing so speeds up the training of our corrective NODE, whereas the NODE training in [43] solves these generally expensive FOM evaluations during their NODE training. Lastly, PINODE was only applied to systems with relatively simple long-time dynamics; systems with substantially higher complexity are considered here.

A summary of the architectures used for all neural networks introduced above is provided in Table II. We emphasize that our physics-informed ROM (MG-N) and hybrid ROMs (PI-DManD-c and PI-DManD-B) are non-intrusive — the MG-N model given by Equation 15, PI-DManD-c model given by Equation 16, and the PI-DManD-B model given by Equation 19 can be constructed from just a time series data set of  $u_i$  and  $f_{\text{FOM},i}$  for  $i = 1, \dots, N$ . However, we note that these three methods are intrusive if  $f_{\text{FOM},i}$  data are not available (e.g. dataset comes from experiments); in this case, the training of the MG-N model (which PI-DManD-c and PI-DManD-B are based on) has a preprocessing step of calculating  $f_{\text{FOM},i}$  from  $u_i$  for all  $i$  (which is relatively fast due to the ability to parallelize the calculation across snapshots). MG is always intrusive though, since one requires direct access to the FOM  $f_{\text{FOM}}$  at each RHS function evaluation when integrating along a trajectory.

Network	Function	Layers	Activations
Encoder	$\mathcal{E}$	$d_u:4d_u:2d_u:d_h$	ReLU:ReLU:Linear
Decoder	$\mathcal{D}$	$d_h:2d_u:4d_u:d_u$	ReLU:ReLU:Linear
NODE (DManD)	$g_d$	$d_h:256:256:d_h$	GeLU:GeLU:Linear
Neural network (MG-N)	$g_{mn}$	$d_h:256:256:d_h$	GeLU:GeLU:Linear
NODE (PI-DManD-c)	$g_c$	$d_h:256:256:d_h$	GeLU:GeLU:Linear
NODE (PI-DManD-B)	$g_B$	$d_h:256:256:d_h$	GeLU:GeLU:Linear

**TABLE II:** Neural network architectures for the autoencoder, DManD, MG-N, and the two PI-DManD-c methods.

## D. Training details

Training is performed in PyTorch [62]. The first 80% of the times series is used for training, and the remaining 20% for testing. For all neural networks, we use an AdamW optimizer with a multistep learning rate scheduler that starts the learning rate at  $10^{-3}$  and halves it 7 times until  $\approx 10^{-5}$ . By default, we use a weight decay of  $10^{-4}$ ; however, for the networks trained in the scarce data case in Section III B we increase the weight decay strength from  $10^{-4}$  to  $10^{-3}$ – $10^0$  (a sweep is done to decide on the value).

For the autoencoder used to learn  $\mathcal{E}$  and decoder  $\mathcal{D}$  (see architectures in Table II), the dimension of the latent space  $h$  needs to be determined. For the KSE system considered in this paper, the dimension of the invariant manifold is known to be  $d_M = 8$  [19, 54, 56, 57]. For the CGLE system considered in the SI, we estimate the dimension of the invariant manifold using an implicit rank-minimizing autoencoder [57, 63] (see Supplementary Section S1 C 1 for details). For the autoencoder, we use a batch size of 64 and train for 2000 epochs. For the neural network used to learn  $g_{mn}(h)$  for MG-N (see architecture in Table II), we use a batch size of 256 and train for 2000 epochs.

The training details for the NODEs  $g_d$ ,  $g_c$ , and  $g_B$  (see architectures in Table II) are as follows. We use the 5th order Dormand-Prince (dopri5) adaptive time-step integrator in the `torchdiffeq` package [64] with default tolerances. For all NODE training, we use a batch size of 64 and train for 100,000 *iterations*. While the terms “iterations” and “epochs” are often used interchangeably in the research community with regards to NODE training, the former is more technically correct and is the nomenclature used in the original NODE paper [52]. The definition of an iteration is to update the weights by randomly sampling a single batch (size 64 in our case) from the entire dataset and performing a forward and backward pass, while a single epoch performs many iterations until the entire dataset is sampled. The published NODE code in [52] uses iterations, so we do too in our adapted code. For training the corrective NODE model  $g_c$  for PI-DManD-c in particular, we use near-zero weight initialization (all other neural network training is with Pytorch’s default Xavier weight initialization); this choice is motivated by the fact that  $g_c$  would be zero if  $g_{mn}$  in Equation 16 were exact (i.e. if there were no FOM approximation error). Lastly, for PI-DManD-B, we use  $\lambda_B = 10^{-5}$  (see Equation 20) for the strength of the regularization

parameter. For the systems considered in this paper, we found that the results (even if the FOM is not exact) are robust to the value of  $\lambda_B$  as long as it is less than  $10^{-3}$ ; in the limit of  $\lambda_B = 0$ , where PI-DManD-B is still robust, the method just involves the transfer learning step of initializing the NODE weights to those of the physics-based prior (which suggests the main benefit of PI-DManD-B comes from the initialization).

## ACKNOWLEDGMENTS

We thank Jake Buzhardt for helpful discussions. This work was supported by the NSF (CBET-2347344) and the ONR (No. N00014-18-1-2865 (Vannevar Bush Faculty Fellowship)).

## S1. SUPPLEMENTARY INFORMATION

### A. Training and testing speed for methods applied to KSE

Here, we examine the cost of training and evaluating each method. As shown in Figure 2(d) of the main text, the NODE  $g_c$  learned by the PI-DManD-c model trains orders of magnitude faster than the DManD model — PI-DManD-c requires only about 10 training iterations for convergence, while DManD requires  $> 10^4$  iterations (PI-DManD-B also takes a similar number of iterations as DManD). However, the PI-DManD-c model adds  $g_c$  to the MG-N model  $g_{mn}$  (see Equation 16), so the time to obtain an MG-N model needs to be considered in addition to the NODE training time. We define training time for the hybrid ROMs as the time needed to obtain a trained MG-N model plus the time needed to train the NODE. We also define training time for MG-N as the network training time plus the time for preprocessing the MG vector field output data from the data of the vector field on the state space (0.1 hours for KSE). Table S1 shows the training time for all methods. One can see that the total time for training either hybrid methods is greater than that of DManD; however, as seen in the last row of Table S1, MG-N and the hybrid methods are comparable to DManD in regards to how fast a test trajectory can be evaluated for 100 Lyapunov times. While MG requires no training time to obtain the vector field on the manifold, it is over an order of magnitude slower to evaluate than the other methods — as discussed in Section V of the Methods in the main text, the reason is that MG needs to decode  $h$ , solve the FOM, and evaluate a Jacobian (which involves an encoding step) for each function evaluation of  $g_m$ . So, MG is clearly not a ROM. Although the MG-N and hybrid methods require a longer time to train than DManD, they all take a similar amount of time to evaluate/test and have the added benefit of substantially better short-time tracking of the true solution.

	DManD	MG-N	MG	PI-DManD-c	PI-DManD-B
Train time (hr)	2.2	8.3	n/a	13.1	12.0
Test time (s)	8.3	8.2	102	11.4	7.7

**TABLE S1:** Comparing computation time for methods applied to KSE. First row is time (in hours) for training. Second row is computation time (in seconds) for testing, where an initial condition is integrated for 100 Lyapunov times. Calculations were run on an Intel Xeon E5-2640 CPU.

## B. Long time statistics results for KSE

Besides the short-time tracking results described in the main text, we also gauge model performance based on how well a predicted trajectory stays on the true attractor at long times. Since for KSE at  $L = 22$  the invariant manifold for the long-time dynamics is 8-dimensional, we simplify the comparison of the long-time statistics by choosing two relevant quantities and calculating a joint probability distribution function (pdf). The time-evolution of the “energy”  $\bar{u^2}/2$ , where  $\bar{\cdot}$  denotes average over the spatial domain, has a growth (“production”) term proportional to  $\|\bar{u_x^2}\|_2$  and a decay (“dissipation”) term proportional to  $\bar{u_{xx}^2}$ , where the subscript  $x$  denotes spatial derivative. Based on this observation, we use the joint pdf of  $u_x$  and  $u_{xx}$  to characterize the attractor. We calculate joint pdfs using the entire testing dataset (100,000 snapshots spaced by  $\tau = 0.25$  time units), where model predictions use the first snapshot as an initial condition. Figure S1(a) shows the joint pdfs for long-time trajectories corresponding to the ground truth, DManD, and PI-DManD-c. The joint pdfs for PI-DManD-B and the two physics-informed methods are not shown since they are virtually identical to the joint pdfs that are shown. To quantitatively compare the pdfs of the model predictions to the pdf of the ground truth trajectory, we calculate the earth mover’s distance (EMD), also known as the Wasserstein-1 distance [65]. Let  $\mu$  and  $\nu$  be two discrete distributions calculated from normalized histograms with  $n_\mu$  and  $n_\nu$  bins, respectively. The EMD between these two distributions is the minimal cost of transforming one distribution

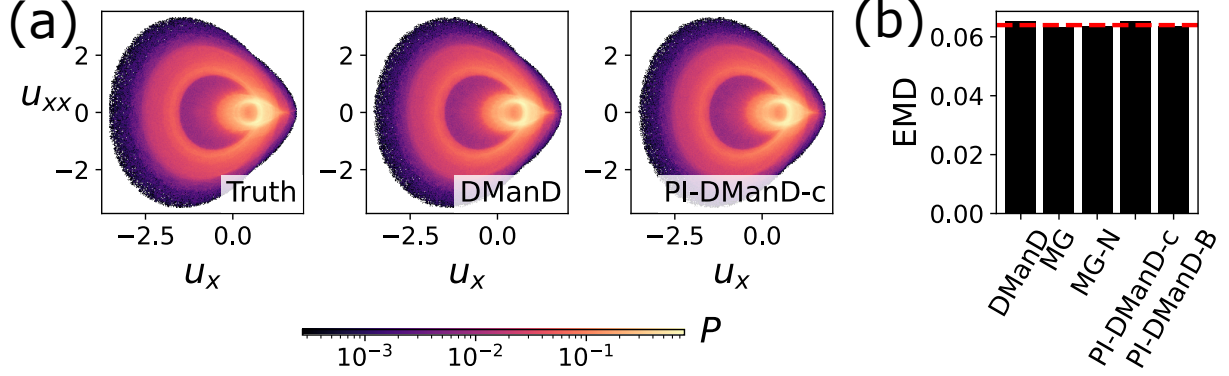


**FIG. S1:** KSE,  $L = 22$  (for both data and FOM),  $N = 400,000$ ,  $\tau = 0.25$ . (a) Comparison of joint pdfs. (b) Earth movers distance (EMD) quantifying the difference between pdfs of the ground truth and model predictions, where the dashed red line is the baseline EMD calculated with the pdf of another ground truth trajectory. Joint pdfs for models not shown look similar to joint pdfs of models with similar EMD values.

to the other, and is given by

$$\text{EMD}(\mu, \nu) = \min_{\gamma} \sum_{i,j} \gamma_{i,j} \|\mu^{(i)} - \nu^{(j)}\|_2 \quad (\text{S1})$$

$$\text{s.t.} \quad \gamma \mathbf{1} = \mu, \quad \gamma^\top \mathbf{1} = \nu, \quad \gamma \geq 0, \quad (\text{S2})$$

where  $\mathbf{1}$  is a column vector of ones and  $\gamma \in \mathbb{R}^{n_\mu \times n_\nu}$  is a transport plan with  $\gamma_{i,j}$  dictating the amount of probability mass to move from bin  $\mu^{(i)}$  to bin  $\nu^{(j)}$ . The EMD represents the minimal work (amount of mass moved multiplied by distance) needed to execute the optimal transport plan. Throughout this paper, the EMD value is calculated with respect to the pdf of the ground truth trajectory in the testing dataset, which we call  $\mu_t$ .

We first show the long-time statistics reconstruction for the case of abundant data and exact FOM (see Section III A of the main text). In Figure S1(b), we plot the EMD between  $\mu_t$  and the model prediction pdf for all five methods. Note that the dashed red line in Figure S1(b) represents the baseline EMD, which is calculated between  $\mu_t$  and the pdf of a ground truth trajectory in the training dataset. Since all methods have a EMD value similar to this baseline EMD, they perform equally well in capturing the long-time statistics, at least for the joint pdf quantities chosen here.

Next, we show the long-time statistics reconstruction for the case of abundant data and inexact FOM (see Section III C of the main text). In Figure S2(a), we plot the joint pdfs

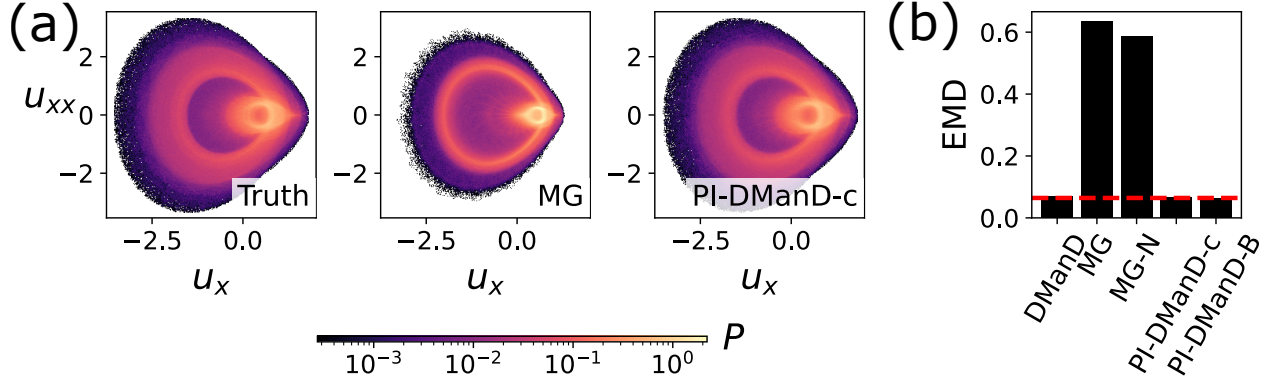


**FIG. S2:** KSE,  $N = 400,000$ ,  $\tau = 0.25$ . Effects of using an erroneous parameter ( $L = 20$ ) in the FOM when making model predictions on the data generated with  $L = 22$ . (a) Comparison of joint pdfs. (b) Earth movers distance (EMD) quantifying the difference between pdfs of the ground truth and model predictions, where the dashed red line is the baseline EMD calculated with the pdf of another ground truth trajectory. Joint pdfs for models not shown look similar to joint pdfs of models with similar EMD values.

for the ground truth trajectory and the MG and PI-DManD-c model predictions. In Figure S2(b), we plot the EMD value (see Equation S2) between pdfs of a model prediction and the ground truth test trajectory; again, the baseline EMD (dashed red line in the figure) is calculated between two ground truth trajectories. (Pdfs for models not shown are similar to shown pdfs if they have similar EMD values.) Figure S2 shows that when given an erroneous parameter value for  $f_{\text{FOM}}$ , MG and MG-N will evolve the  $L = 22$  dataset on a completely incorrect attractor. As for the two hybrid methods, they capture the long-time statistics as well as DManD.

### C. Complex Ginzburg–Landau Equation

In addition to the KSE, we have studied PI-DManD for prediction of dynamics of the one-dimensional complex Ginzburg–Landau equation (CGLE) [49]

$$\frac{\partial A}{\partial t} = A + (1 + i\alpha) \frac{\partial^2 A}{\partial x^2} - (1 + i\beta)|A|^2 A. \quad (\text{S3})$$

The quantities  $\alpha$  and  $\beta$  are parameters. We use a domain length  $L = 30$  and periodic boundary conditions. We set  $\alpha = 2$  and  $\beta = -2$ , so when  $L = 30$  the dynamics lie in the ‘‘defect-mediated turbulence’’ regime [50]. The solution is computed with an ETD-

RK4 solver [58] in the Fourier domain. We used the Bennitin algorithm [66] to determine a Lyapunov time of 2.8 time units. With the initial transient removed, we generate  $10^5$  snapshots of  $A \in \mathbb{C}^{64}$  discretized on  $d_u = 64$  uniformly spaced grid points and separated by  $\tau = 0.05$  time units (note,  $\tau$  is five times smaller here for the CGLE compared to the KSE). To work with real numbers in our neural networks, we concatenate the real and imaginary parts of  $A$  to form  $u \in \mathbb{R}^{128}$ . We use  $u$  when calculating error quantities.

### 1. Determining manifold dimension

Unlike the KSE system considered previously, the dimension of the invariant manifold  $d_{\mathcal{M}}$  for data on the attractor for this CGLE system is not known. To estimate it, we use an implicit rank-minimizing autoencoder with weight decay (IRMAE-WD) [57, 63]. IRMAE-WD uses an intermediate latent space  $z \in \mathbb{R}^{d_z}$ , where  $d_z$  acts as an upper bound on the manifold dimension (we use  $d_z = 50$  here). The difference between IRMAE-WD and a normal AE is the use of linear layers in the former, which act to drive the covariance matrix  $zz^T$  to have minimal rank  $d_{\mathcal{M}} < d_z$ . IRMAE-WD has been applied to the KSE in [57], where the singular value spectra of  $zz^T$  contains a sharp drop-off that spans over 10 orders of magnitude — this clear indication of the rank of  $zz^T$  then gives us an estimate of the manifold dimension  $d_{\mathcal{M}}$ .

We train an IRMAE-WD autoencoder on the CGLE system with weight-decay strength  $10^{-5}$  and four linear layers. Figure S3 shows the singular value spectra, where the sharp drop-off covering about 10 orders of magnitude occurring at the 40th singular value index indicates that our data has  $d_{\mathcal{M}} = 40$ . The IRMAE-WD relative reconstruction error (calculated with Equation 6 in the main text) is  $\epsilon_{\text{AE}} = 0.61\%$ . Note that we observed similarly sharp drop-offs at singular value indices ranging from 33 to 39 for 4 other IRMAE models. Therefore, we choose an estimate that is at the high end (40) of an ensemble of estimates.

Before using the IRMAE-WD in a ROM, we would need to project the intermediate latent space  $z \in \mathbb{R}^{50}$  onto a latent space  $h \in \mathbb{R}^{40}$  (e.g. with a singular value decomposition); however, doing so would make the encoder  $\mathcal{E} : u \rightarrow h$  more complicated. Therefore, to simplify the encoder structure whose Jacobian  $J_{\mathcal{E}}(h)$  must be computed for MG, we choose to instead train and use a normal AE with latent dimension  $d_h = 40$ . The relative reconstruction

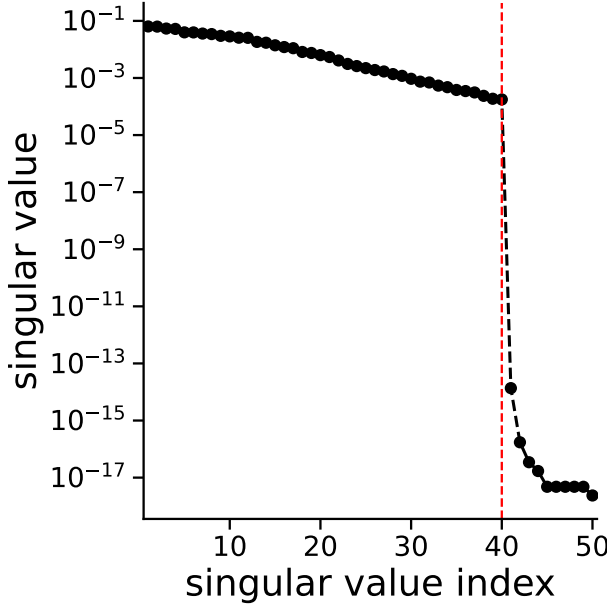


**FIG. S3:** Singular value spectra of the covariance of the latent space  $z$  for IRMAE-WD applied to CGLE. Red dashed line located at 40th singular value index.

error for this normal AE is  $\epsilon_{\text{AE}} = 0.57\%$ , which is similar to that of the IRMAE-WD autoencoder. All of the training details — such as neural network architectures and learning rate scheduling — are identical to those for the KSE, which are shown in Table II of the main text and described in the body of Section VD in the Methods of the main text.

## 2. Abundant data, exact FOM

We begin presentation of the results by paralleling the KSE results of Section III A, using the entire dataset of  $N = 400,000$  training snapshots spaced apart by  $\tau = 0.05$  time units and using the same parameters  $\alpha = 2$  and  $\beta = -2$  for data generation and the FOM. Figure S4(a) shows the ensemble-averaged tracking error for all methods. The physics-informed MG-N method (whose curve is directly underneath the red PI-DManD-c curve in Figure S4(a)) and the two hybrid methods outperform DManD in short-time tracking; while this result is consistent with the KSE results in Figure 2(a), the primary difference here is that MG has dramatically lower short-time tracking error. As shown in the representative space-time plots in Figure S4(b) and the difference plots in Figure S4(c), MG is tracking the true solution with very small error for 3 Lyapunov times. For KSE, the short-time tracking error

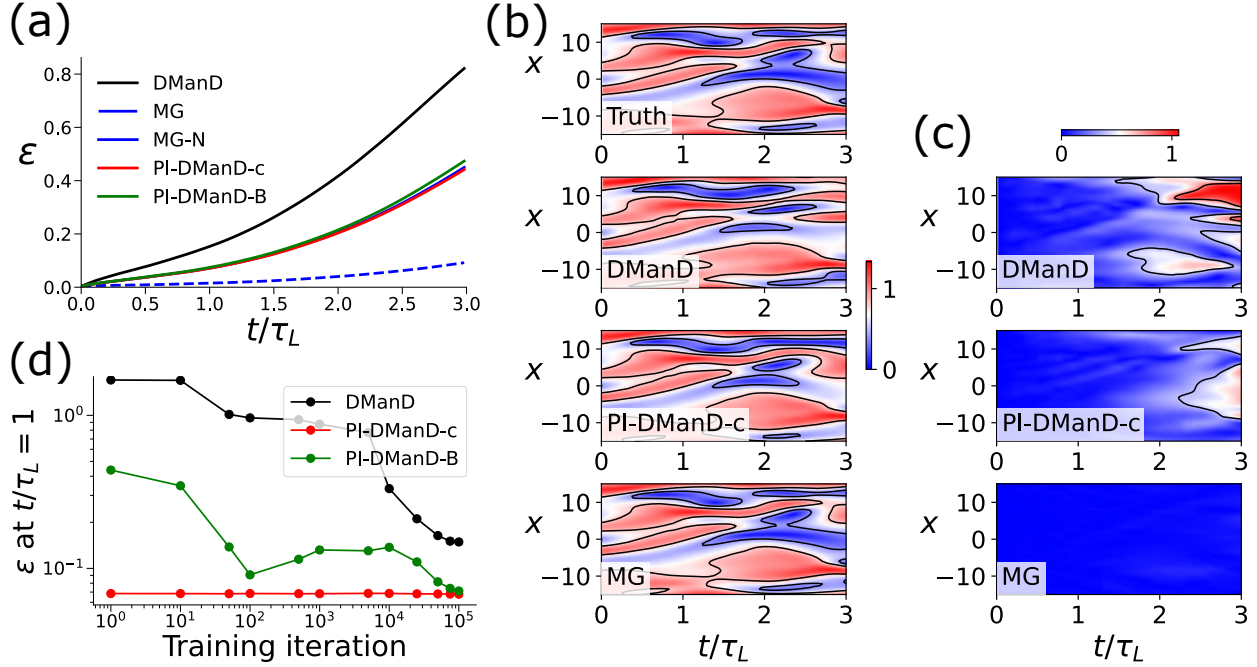


**FIG. S4:** CGLE,  $\beta = -2$  (for both data and FOM),  $N = 400,000$ ,  $\tau = 0.05$ . (a) Ensemble-averaged short-time tracking error for all methods. (b) Absolute value of representative trajectories of ground truth and model predictions (contours at  $|A| = 0.4, 0.8$ ). (c) Difference plots between ground truth and model predictions (contours at difference values of 0.4, 0.8). Representative trajectories and difference plots for other models look similar to those of PI-DManD-c. (d) NODE training convergence for purely data-driven and hybrid methods.

at one Lyapunov time is about 0.07 for both MG and MG-N; however, for CGLE, it is about 0.07 for MG-N and about 0.02 for MG. We believe that the gap in the error between MG and MG-N is larger for the CGLE case due to a higher error in approximating  $g_m$  with  $g_{mn}$  ( $\epsilon_{\text{MG-N}}$  is 8% for CGLE and 2.3% for KSE).

The superior predictive performance of MG for the CGLE comes at a large cost. In Table S2, we show the training and testing time for all methods (analogous to Table S1 for the KSE in Section III A). Here, MG still takes almost two orders of magnitude longer to evolve a trajectory. Figure 2(d) shows the NODE training convergence, where the results are as before with the NODE  $g_c$  learned by the PI-DManD-c model training orders of magnitude faster than the DManD model. However, when accounting for the training cost of the MG-N network  $g_{mn}$  (which includes 0.15 hours of preprocessing time), the total cost for training both  $g_c$  and  $g_{mn}$  for PI-DManD-c is greater than for DManD (see Table S2).

We now determine whether long-time trajectories of each method stay on the true CGLE

	DMaND	MG-N	MG	PI-DMaND-c	PI-DMaND-B
Train time (hr)	2.2	9.3	n/a	13.0	12.3
Test time (s)	4.9	5.0	218.0	6.8	4.5

**TABLE S2:** Comparing computation time for methods applied to CGLE. First row is time (in hours) for training. Second row is computation time (in seconds) for testing, where an initial condition is integrated for 100 Lyapunov times. Calculations were run on an Intel Xeon E5-2640 CPU.

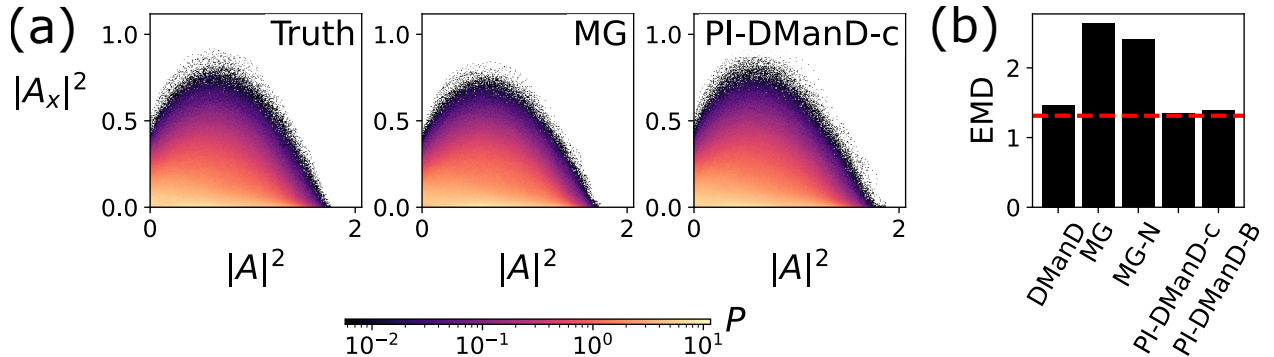


**FIG. S5:** CGLE,  $\beta = -2$  (for both data and FOM),  $N = 400,000$ ,  $\tau = 0.05$ . (a) Comparison of joint pdfs. (b) Earth movers distance (EMD) quantifying the difference between pdfs of the ground truth and model predictions, where the dashed red line is the baseline EMD calculated with the pdf of another ground truth trajectory. Joint pdfs for models not shown look similar to joint pdfs of models with similar EMD values.

attractor. As with the KSE, we will calculate a joint pdf to use as a simple metric for the long-time statistics. We again performed a kinetic energy ( $|A|^2$ ) balance on the PDE, which yielded a production term  $\overline{|A|^2}$  and a dissipation term  $\overline{|A_x|^2 + |A|^4}$ , where  $A_x$  is a spatial derivative; from these terms, we choose the joint pdf quantities as  $|A|^2$  and  $|A_x|^2$ , respectively. The joint pdfs for the ground truth, DMaND and PI-DMaND-c model predictions are shown in Figure S4(a), while the EMD (see Equation S2) calculated between all methods and the ground truth trajectory is presented in Figure S4(b). As before, the baseline EMD for the dashed red line is calculated between ground truth trajectories with different initial conditions. All methods have a similar EMD to this baseline, so they perform equally well in capturing the long-time statistics of these quantities.

### 3. Scarce data, exact FOM

Here, we parallel the KSE results of Section III B of the main text. As with the KSE, we use the exact FOM and study the effect of having less data (training data size  $N < 400,000$ ), data spaced further apart ( $\tau > 0.05$ ), or both simultaneously.

We first fix the data spacing at  $\tau = 0.05$  and vary the training data size from  $N = 400,000$  to 100,000, 25,000, and 10,000 (i.e. shorter time series). Figure S6a shows the ensemble-averaged tracking error  $\epsilon$  at one Lyapunov time for decreasing  $N$  (the case of  $N = 400,000$  corresponds to Figure S4). Similar to the KSE, here the NODE test error  $\epsilon$  increases with decreasing  $N$  for all methods due to increasing AE reconstruction error  $\epsilon_{\text{AE}}$ . The AE errors  $\epsilon_{\text{AE}}$  and MG-N errors  $\epsilon_{\text{MG-N}}$  here are higher than they were for the KSE, but the NODE errors  $\epsilon$  are about the same for both datasets. Another difference is that for  $N = 100,000$ , PI-DManD-B (but not PI-DManD-c) is able to achieve error that is substantially lower than that of MG-N, which suggests the hybrid ROM is correcting for MG-N test error.

The second scenario is using a fixed number of training snapshots  $N = 400,000$  and increasing the data spacing from  $\tau = 0.05$  to 0.2, 1, and 2 (i.e. use time series that are longer and sampled less often as  $\tau$  increases). Figure S6b shows the errors for this scenario. As with the KSE, here the AE, MG-N, and NODE errors do not vary much with  $\tau$ . Note that the missing PI-DManD-c bars in Figure S6(b), denoted with asterisk, have an error of about 1 and are omitted to improve clarity in the vertical axis. The reason is that  $\tau = 1$  time units corresponds to about one third of a Lyapunov time, so PI-DManD-c struggles in short-time tracking in this case and for  $\tau = 2$ . Across the three increased  $\tau$  values, both hybrid ROMs have lower error than DManD (except  $\tau = 1$  and 2, where only PI-DManD-B does).

Lastly, we study the effect of both increasing the data spacing  $\tau$  and decreasing the number of training snapshots  $N$  (i.e. downsampling the original time series of length  $N = 400,000$  and  $\tau = 0.05$ ). In Figure S6(c), we show the tracking error for data spacing  $\tau = 0.2, 1$ , and 2 with  $N$  decreasing proportionally. The tracking error  $\epsilon$  increases for all methods with increasing  $\tau$  due to the increasing AE error  $\epsilon_{\text{AE}}$ . (As with the KSE, the PI-DManD-c error for  $\tau = 2$  and  $N = 10,000$  is around 1 and is omitted from Figure S6(c) to improve the clarity in the scaling of the vertical axis.) As with the KSE, the tracking errors for MG, MG-N, and PI-DManD-c become larger than that of DManD. For the KSE results in Figure

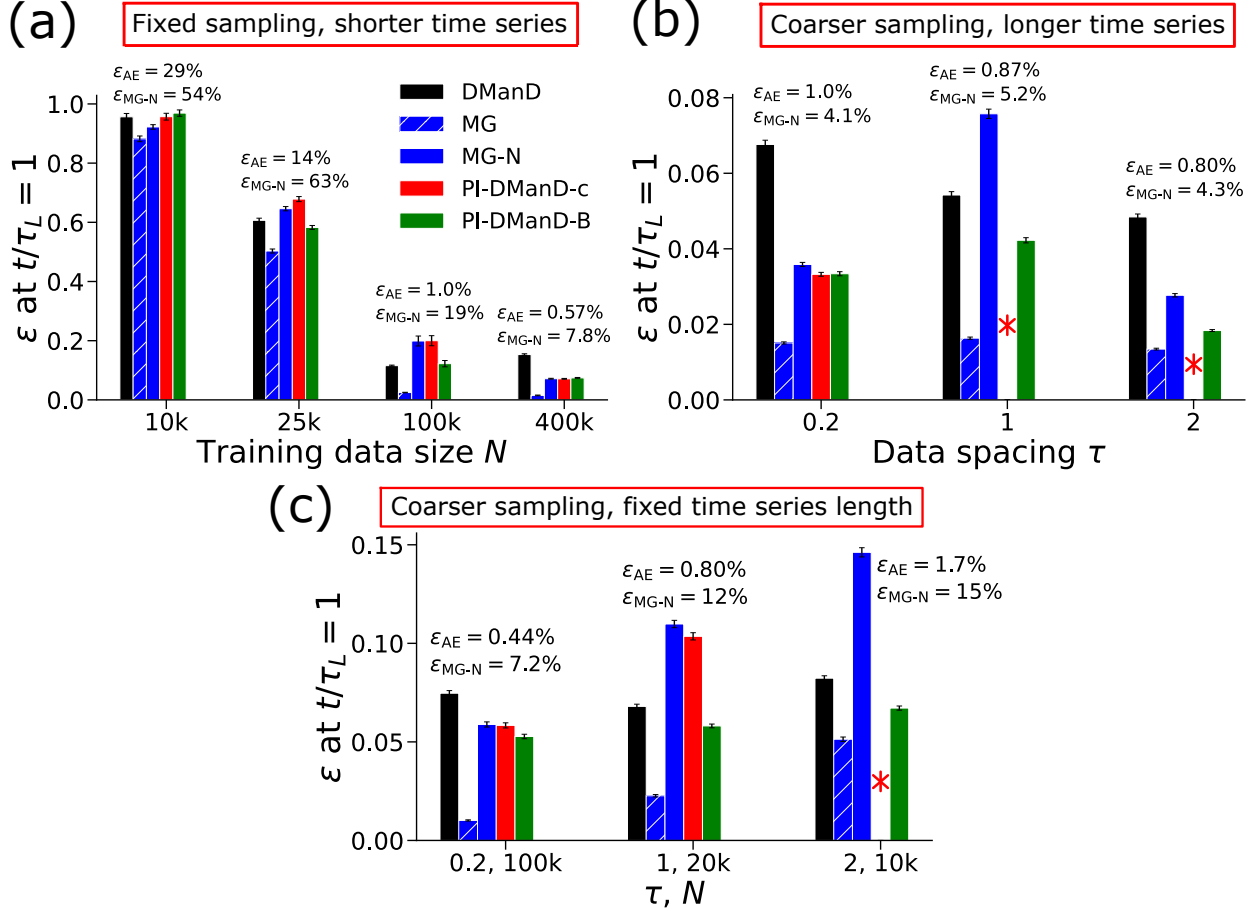


**FIG. S6:** CGLE,  $\beta = -2$  (for both data and FOM). Short-time tracking error at one Lyapunov time for scarce data in terms of (a) less data with  $N \leq 400,000$  and  $\tau = 0.05$  (i.e. shorter time series), (b) widely spaced data with  $\tau > 0.05$  and  $N = 400,000$ , and (c) increasing  $\tau$  and decreasing  $N$  proportionally. Error bars are standard errors, and all subplots follow the legend in (a). Note the different vertical axis limits for each subplot. Missing PI-DManD-c bars, denoted with asterisk, in (b) and (c) have errors of about 1 and are omitted to improve clarity in vertical axis.

3(c) in the main text, the PI-DManD-B error remained comparable to DManD error for two out of the three values of  $\tau$  and was slightly less than the DManD error for the other value of  $\tau$ ; here, however, PI-DManD-B has somewhat lower error than DManD for all three values of  $\tau$ . As with the KSE, across the three cases of data-scarce training, PI-DManD-B always has equal or lower error than DManD while PI-DManD-c sometimes has a higher error.

#### 4. Erroneous FOM

We now test how well the hybrid methods can perform despite being informed with a FOM containing erroneous parameters. The results here parallel the KSE results in Section III C in the main text. We create a hybrid ROM for evolving the dataset generated with the correct parameters  $\alpha = 2$  and  $\beta = -2$  when provided a FOM  $f_{\text{FOM}}$  with  $\beta = -1.8$  or  $\beta = -1$  (holding  $\alpha = 2$ ). For both  $\beta = -2$  and  $\beta = -1.8$ , the dynamics lie in the defect-mediated turbulence regime [50]; however, for  $\beta = -1$ , the dynamics instead lie in the phase-turbulence regime [50]; example trajectories for these three values of  $\beta$  are shown in Figure S7(a). It bears repeating that the two erroneous  $\beta$  values are only used in the  $f_{\text{FOM}}(u; \mu_{\text{FOM}})$  term in Equation 13 of MG (which also affects  $g_{mn}$  learned by MG-N) — no dataset is generated with the erroneous  $\beta$  values.

We first compare short-time tracking performance. Figures S7(b) and S7(c) show the tracking error of all methods for  $\beta = -1.8$  and  $\beta = -1$ , respectively. Unsurprisingly, the value of  $\beta$  used in the FOM does not affect the predictive capability of DManD, since it does not use any prior knowledge of the physics. As was the case with KSE  $L = 20$  in Figure 4, MG and MG-N here also poorly track the true solution due to being informed with erroneous FOM parameters. (Note, the curves for MG and MG-N in Figure S7(c) level off to around 1.5, and the vertical axis limits are shrunk to provide clarity.) As the accuracy of the prior decreases ( $\beta$  strays further away from  $-2$ ), the tracking error for PI-DManD-c and PI-DManD-B grow slightly but still remain lower than the error for DManD; however, the tracking error for PI-DManD-B is noticeably lower than that of PI-DManD-c for  $\beta = -1$ , which is in line with the KSE results in Section IIIC where only PI-DManD-B maintained a lower tracking error than DManD. Importantly, across both spatiotemporally chaotic datasets, the results show that including knowledge of the physics (even if inaccurate) helps in creating hybrid ROMs (PI-DManD-B especially) that perform better than solely data-driven ROMs (DManD) in short-time predictions.

Lastly, we investigate the long-time statistics of the model predictions by calculating the joint pdf of quantities  $|A|^2$  and  $|A_x|^2$ . We plot the joint pdfs for the ground truth trajectory and the MG and PI-DManD-c model predictions in Figure S8(a) for  $\beta = -1.8$ . The EMD values (see Equation S2) between pdfs of a model prediction and the ground truth

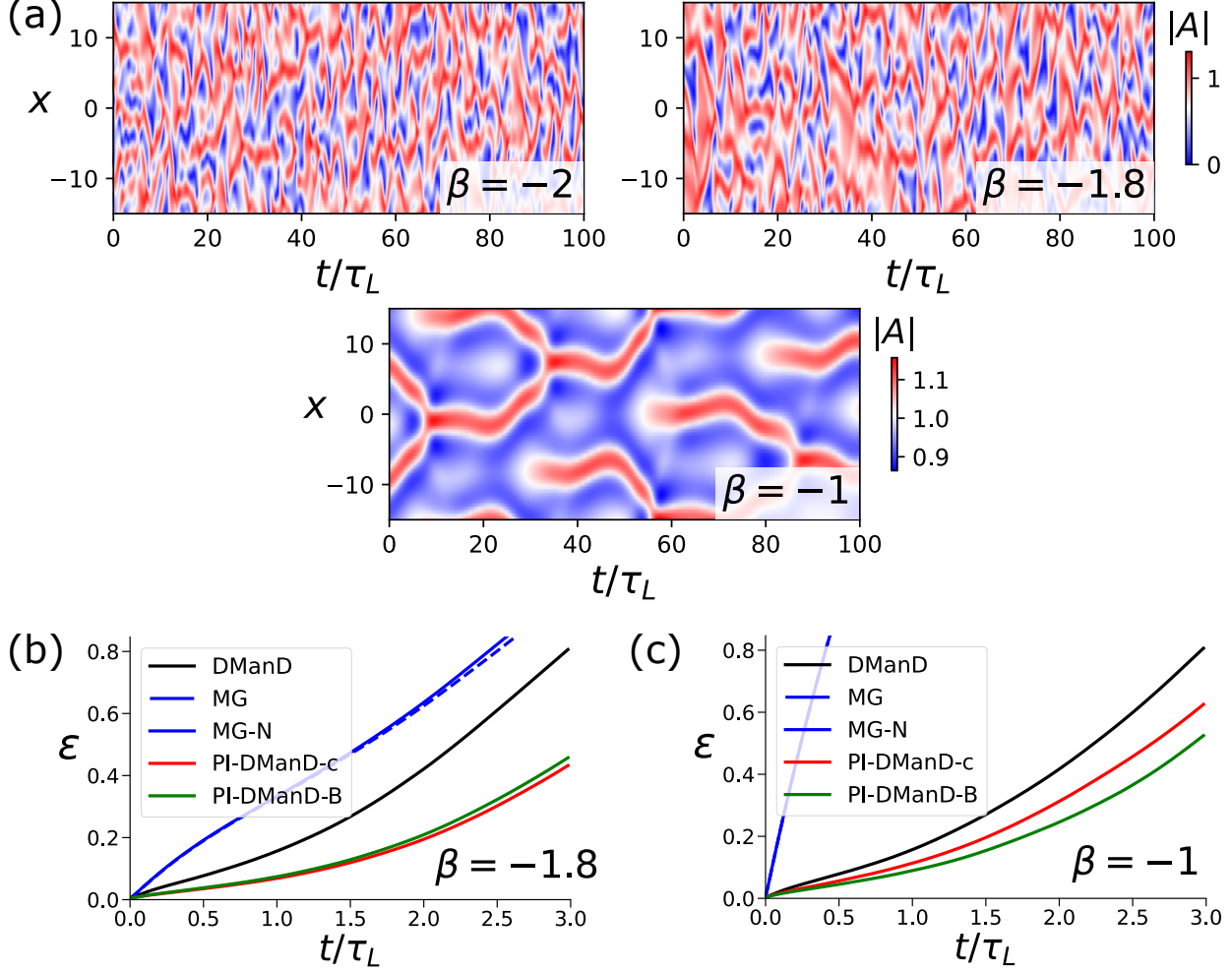


**FIG. S7:** CGLE,  $N = 400,000$ ,  $\tau = 0.05$ . Effects of using an erroneous parameter ( $\beta = -1.8$  or  $\beta = -1$ ) in the FOM to model data generated with  $\beta = -2$ . (a) Ground truth trajectory (top-left) and example trajectories for the two erroneous  $\beta$  values (top-right and bottom); note the different colorbar axis limits. Ensemble-averaged short-time tracking error when using  $\beta = -1.8$  (b) or  $\beta = -1$  (c) in the FOM.

test trajectory are provided in Figure S8(b). (Again, the baseline EMD represented by the dashed red line in a bar plot is calculated between two ground truth trajectories, and pdfs for models not shown are similar to shown pdfs if they have similar EMD values.) For  $\beta = -1$ , we report (but not show to reduce redundancy) that the EMD values for MG and MG-N were larger than 40 while the EMD values for the other three methods were as close to the baseline EMD of around 1.3 as for the  $\beta = -1.8$  case. When given an erroneous parameter value for the FOM, the two physics-informed MG and MG-N methods evolve the  $\beta = -2$  dataset with a completely incorrect vector field, leading to poor reconstruction of long-time

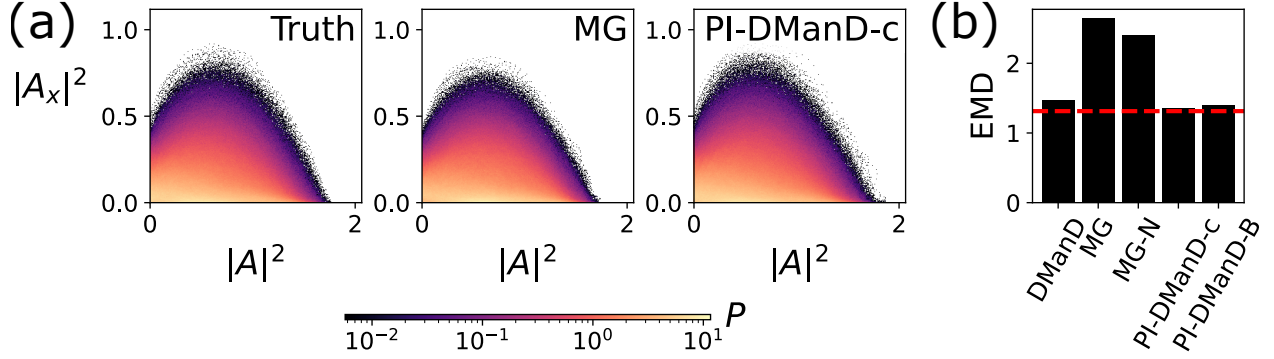


**FIG. S8:** CGLE,  $N=400,000$ ,  $\tau = 0.05$ . Effects of using an erroneous parameter ( $\beta = -1.8$ ) in the FOM to model the data generated with  $\beta = -2$ . (a) Comparison of joint pdfs for  $\beta = -1.8$ . (b) Earth movers distance (EMD) quantifying the difference between pdfs of the ground truth and model predictions for  $\beta = -1.8$ . Dashed red line is the baseline EMD calculated with the pdf of another ground truth trajectory. Joint pdfs for models not shown look similar to joint pdfs of models with similar EMD values.

statistics — this observation is more pronounced for the case of  $\beta = -1$ . As for the two hybrid methods, they capture the long-time statistics of these quantities about as well as DManD.

---

[1] P. Holmes, J. L. Lumley, G. Berkooz, and C. W. Rowley. *Turbulence, Coherent Structures, Dynamical Systems and Symmetry*. Cambridge Monographs on Mechanics. Cambridge University Press, 2 edition, 2012.

[2] R Smith Troy, Moehlis Jeff, and Holmes Philip. Low-Dimensional Modelling of Turbulence Using the Proper Orthogonal Decomposition: A Tutorial. *Nonlinear Dynamics*, (1024):275–307, 2005.

[3] J. F. Gibson. *Dynamical systems models of wall-bounded, shear-flow turbulence*. PhD thesis, Cornell University, January 2002.

[4] Roger Temam. Infinite-dimensional dynamical systems in mechanics and physics. 68, 1997.

[5] S. V. Zelik. Attractors. then and now. *Russian Mathematical Surveys*, 78:635–777, 8 2022.

[6] G. E. Hinton and R. R. Salakhutdinov. Reducing the dimensionality of data with neural networks. *Science*, 313(5786):504–507, 2006.

[7] Ian Goodfellow, Yoshua Bengio, and Aaron Courville. *Deep Learning*. MIT Press, 2016.

<http://www.deeplearningbook.org>.

- [8] Michele Milano and Petros Koumoutsakos. Neural network modeling for near wall turbulent flow. *Journal of Computational Physics*, 182(1):1–26, 2002.
- [9] A. Solera-Rico, C. S. Vila, M. Gómez-López, Y. Wang, A. Almashjary, S. T. M. Dawson, and R. Vinuesa.  $\beta$ -Variational autoencoders and transformers for reduced-order modelling of fluid flows. *Nature Communications*, 15(1):1361, 2024.
- [10] Noriyasu Omata and Susumu Shirayama. A novel method of low-dimensional representation for temporal behavior of flow fields using deep autoencoder. *AIP Advances*, 9(1):015006, 2019.
- [11] Eleni D. Koronaki, Nikolaos Evangelou, Cristina P. Martin-Linares, Edriss S. Titi, and Ioannis G. Kevrekidis. Nonlinear dimensionality reduction then and now: AIMs for dissipative PDEs in the ML era. *Journal of Computational Physics*, 506:112910, 2024.
- [12] Kookjin Lee and Kevin T. Carlberg. Model reduction of dynamical systems on nonlinear manifolds using deep convolutional autoencoders. *Journal of Computational Physics*, 404:108973, 2020.
- [13] Ricky T. Q. Chen, Yulia Rubanova, Jesse Bettencourt, and David Duvenaud. Neural ordinary differential equations. *arXiv preprint*, 2019.
- [14] Pantelis R. Vlachas, Georgios Arampatzis, Caroline Uhler, and Petros Koumoutsakos. Multiscale simulations of complex systems by learning their effective dynamics. *Nature Machine Intelligence*, 4(4):359–366, 2022.
- [15] Romit Maulik, Bethany Lusch, and Prasanna Balaprakash. Reduced-order modeling of advection-dominated systems with recurrent neural networks and convolutional autoencoders. *Physics of Fluids*, 33, 3 2021.
- [16] Andrew L. Ferguson, Athanassios Z. Panagiotopoulos, Ioannis G. Kevrekidis, and Pablo G. Debenedetti. Nonlinear dimensionality reduction in molecular simulation: The diffusion map approach. *Chemical Physics Letters*, 509(1-3):1–11, 2011.
- [17] Mattia Cenedese, Joar Axås, Bastian Bäuerlein, Kerstin Avila, and George Haller. Data-driven modeling and prediction of non-linearizable dynamics via spectral submanifolds. *Nature Communications*, 13:872, 2 2022.
- [18] A. Liu, J. Axås, and G. Haller. Data-driven modeling and forecasting of chaotic dynamics on inertial manifolds constructed as spectral submanifolds. *Chaos*, 34(3):033140, 03 2024.

- [19] Alec J. Linot and Michael D. Graham. Deep learning to discover and predict dynamics on an inertial manifold. *Phys. Rev. E*, 101:062209, 2020.
- [20] Alec J. Linot, Joshua W. Burby, Qi Tang, Prasanna Balaprakash, Michael D. Graham, and Romit Maulik. Stabilized neural ordinary differential equations for long-time forecasting of dynamical systems. *Journal of Computational Physics*, 474:111838, 2023.
- [21] Alec J. Linot, Kevin Zeng, and Michael D. Graham. Turbulence control in plane Couette flow using low-dimensional neural ODE-based models and deep reinforcement learning. *International Journal of Heat and Fluid Flow*, 101:109139, 2023.
- [22] Carlos E. Pérez De Jesús and Michael D. Graham. Data-driven low-dimensional dynamic model of Kolmogorov flow. *Physical Review Fluids*, 8(4):044402, 2023.
- [23] Alec J. Linot and Michael D. Graham. Data-driven reduced-order modeling of spatiotemporal chaos with neural ordinary differential equations. *Chaos: An Interdisciplinary Journal of Nonlinear Science*, 32(7):073110, 2022.
- [24] Charles D. Young and Michael D. Graham. Deep learning delay coordinate dynamics for chaotic attractors from partial observable data. *Physical Review E*, 107(3):034215, 2023.
- [25] Daniel Floryan and Michael D. Graham. Data-driven discovery of intrinsic dynamics. *Nature Machine Intelligence*, 4:1113–1120, 2022.
- [26] Kevin Zeng and Michael D. Graham. Symmetry reduction for deep reinforcement learning active control of chaotic spatiotemporal dynamics. *Physical Review E*, 104:014210, 2021.
- [27] Alec J Linot and Michael D Graham. Deep learning to discover and predict dynamics on an inertial manifold. *Physical Review E*, 101(6):062209, 06 2020.
- [28] Andrew J. Fox, C. Ricardo Constante-Amores, and Michael D. Graham. Predicting extreme events in a data-driven model of turbulent shear flow using an atlas of charts. *Physical Review Fluids*, 8(9):094401, 2023.
- [29] Kevin Zeng, Alec J. Linot, and Michael D. Graham. Data-driven control of spatiotemporal chaos with reduced-order neural ODE-based models and reinforcement learning. *Proceedings of the Royal Society A*, 478(2267):20220297, 2022.
- [30] Carlos E Pérez De Jesús, Alec J Linot, and Michael D Graham. Building symmetries into data-driven manifold dynamics models for complex flows. *arXiv*, 2023.
- [31] Carlos E. Pérez De Jesús and Michael D. Graham. Data-driven low-dimensional dynamic

model of Kolmogorov flow. *Physical Review Fluids*, 8(4):044402, 2023.

[32] Carlos E. Pérez De Jesús, Alec J. Linot, and Michael D. Graham. Building symmetries into data-driven manifold dynamics models for complex flows. *Physical Review Fluids*, 2025.

[33] Alec J Linot and Michael D Graham. Dynamics of a data-driven low-dimensional model of turbulent minimal Couette flow. *arXiv*, 2023.

[34] M Raissi, P Perdikaris, and G E Karniadakis. Physics-informed neural networks: A deep learning framework for solving forward and inverse problems involving nonlinear partial differential equations. *Journal of Computational Physics*, 378:686 – 707, 2019.

[35] George Em Karniadakis, Ioannis G. Kevrekidis, Lu Lu, Paris Perdikaris, Sifan Wang, and Liu Yang. Physics-informed machine learning. *Nature Reviews Physics*, 3(6):422–440, 2021.

[36] Maziar Raissi, Paris Perdikaris, and George Em Karniadakis. Physics informed deep learning (part ii): Data-driven discovery of nonlinear partial differential equations. 11 2017.

[37] Sifan Wang, Hanwen Wang, and Paris Perdikaris. Learning the solution operator of parametric partial differential equations with physics-informed deepnets. *Science Advances*, 7, 10 2021.

[38] Zongyi Li, Hongkai Zheng, Nikola Kovachki, David Jin, Haoxuan Chen, Burigede Liu, Kamayyar Azizzadenesheli, and Anima Anandkumar. Physics-informed neural operator for learning partial differential equations. *ACM / IMS Journal of Data Science*, 1:1–27, 9 2024.

[39] Lu Lu, Pengzhan Jin, Guofei Pang, Zhongqiang Zhang, and George Em Karniadakis. Learning nonlinear operators via deeponet based on the universal approximation theorem of operators. *Nature Machine Intelligence*, 3:218–229, 3 2021.

[40] Zongyi Li, Nikola Kovachki, Kamayyar Azizzadenesheli, Burigede Liu, Kaushik Bhattacharya, Andrew Stuart, and Anima Anandkumar. Fourier neural operator for parametric partial differential equations. *ICLR 2021 Workshop on Integration of Deep Neural Models and Differential Equations*, 10 2020.

[41] Jungeun Kim, Kookjin Lee, Dongeun Lee, Sheo Yon Jhin, and Noseong Park. Dpm: A novel training method for physics-informed neural networks in extrapolation. *35th AAAI Conference on Artificial Intelligence, AAAI 2021*, 9B:8146–8154, 12 2020.

[42] Francesco Romor, Giovanni Stabile, and Gianluigi Rozza. Non-linear manifold reduced-order models with convolutional autoencoders and reduced over-collocation method. *Journal of Scientific Computing*, 94:1–39, 3 2023.

[43] Aleksei Sholokhov, Yuying Liu, Hassan Mansour, and Saleh Nabi. Physics-informed neural ode (pinode): embedding physics into models using collocation points. *Scientific Reports*, 13:10166, 6 2023.

[44] Jaideep Pathak, Alexander Wikner, Rebeckah Fussell, Sarthak Chandra, Brian R. Hunt, Michelle Girvan, and Edward Ott. Hybrid forecasting of chaotic processes: Using machine learning in conjunction with a knowledge-based model. *Chaos*, 28(4), 2018.

[45] Pantelis R. Vlachas, Wonmin Byeon, Zhong Y. Wan, Themistoklis P. Sapsis, and Petros Koumoutsakos. Data-driven forecasting of high-dimensional chaotic systems with long short-term memory networks. *Proceedings of the Royal Society A: Mathematical, Physical and Engineering Sciences*, 474(2213):20170844, 2018.

[46] P.R. Vlachas, J. Pathak, B.R. Hunt, T.P. Sapsis, M. Girvan, E. Ott, and P. Koumoutsakos. Backpropagation algorithms and reservoir computing in recurrent neural networks for the forecasting of complex spatiotemporal dynamics. *Neural Networks*, 126:191–217, 2020.

[47] Qingsong Wen, Tian Zhou, Chaoli Zhang, Weiqi Chen, Ziqing Ma, Junchi Yan, and Liang Sun. Transformers in time series: A survey. *IJCAI International Joint Conference on Artificial Intelligence*, 2023-August:6778–6786, 2023.

[48] William Gilpin. Model scale versus domain knowledge in statistical forecasting of chaotic systems. *Physical Review Research*, 5:043252, 10 2023.

[49] Igor S. Aranson and Lorenz Kramer. The world of the complex Ginzburg-Landau equation. *Reviews of Modern Physics*, 74(1):99–143, 2002.

[50] B. I. Shraiman, A. Pumir, W. van Saarloos, P. C. Hohenberg, H. Chaté, and M. Holen. Spatiotemporal chaos in the one-dimensional complex ginzburg-landau equation. *Physica D: Nonlinear Phenomena*, 57:241–248, 8 1992.

[51] Geoffrey Hinton and Sam Roweis. Stochastic neighbor embedding. *Advances in neural information processing systems*, 15:833–840, 2003.

[52] Ricky TQ Chen, Yulia Rubanova, Jesse Bettencourt, and David K Duvenaud. Neural ordinary differential equations. *Advances in neural information processing systems*, 31, 2018.

[53] Hong Liu Yang, Kazumasa A. Takeuchi, Francesco Ginelli, Hugues Chaté, and Günter Radons. Hyperbolicity and the effective dimension of spatially extended dissipative systems. *Physical Review Letters*, 102(7):1–4, 2009.

[54] X. Ding, H. Chaté, P. Cvitanović, E. Siminos, and K. A. Takeuchi. Estimating the Dimension of an Inertial Manifold from Unstable Periodic Orbits. *Physical Review Letters*, 117(2):1–5, 2016.

[55] Russell A. Edson, J. E. Bunder, Trent W. Mattner, and A. J. Roberts. Lyapunov exponents of the Kuramoto–Sivashinsky PDE. *The ANZIAM Journal*, 61(3):270–285, 2019.

[56] Alec J. Linot and Michael D. Graham. Data-driven reduced-order modeling of spatiotemporal chaos with neural ordinary differential equations. *Chaos: An Interdisciplinary Journal of Nonlinear Science*, 32(7):073110, 2022.

[57] K. Zeng, C. E Pérez-De-Jesús, A. J Fox, and M. D Graham. Autoencoders for discovering manifold dimension and coordinates in data from complex dynamical systems. *MLST*, 5(2):025053, may 2024.

[58] Aly-Khan Kassam and Lloyd N. Trefethen. Fourth-order time-stepping for stiff PDEs. *SIAM Journal on Scientific Computing*, 26(4):1214–1233, 2005.

[59] Jake Buzhardt, C. Ricardo Constante-Amores, and Michael D. Graham. On the relationship between koopman operator approximations and neural ordinary differential equations for data-driven time-evolution predictions. *Chaos: An Interdisciplinary Journal of Nonlinear Science*, 35, 4 2025.

[60] Qianxiao Li, Felix Dietrich, Erik M. Boltt, and Ioannis G. Kevrekidis. Extended dynamic mode decomposition with dictionary learning: A data-driven adaptive spectral decomposition of the Koopman operator. *Chaos: An Interdisciplinary Journal of Nonlinear Science*, 27(10):103111, 07 2017.

[61] Alec J. Linot, Joshua W. Burby, Qi Tang, Prasanna Balaprakash, Michael D. Graham, and Romit Maulik. Stabilized neural ordinary differential equations for long-time forecasting of dynamical systems. *Journal of Computational Physics*, 474:111838, 2023.

[62] Adam Paszke, Sam Gross, Francisco Massa, Adam Lerer, James Bradbury, Gregory Chanan, Trevor Killeen, Zeming Lin, Natalia Gimelshein, Luca Antiga, Alban Desmaison, Andreas Kopf, Edward Yang, Zachary DeVito, Martin Raison, Alykhan Tejani, Sasank Chilamkurthy, Benoit Steiner, Lu Fang, Junjie Bai, and Soumith Chintala. Pytorch: An imperative style, high-performance deep learning library. In *Advances in Neural Information Processing Systems 32*, pages 8024–8035. Curran Associates, Inc., 2019.

- [63] L. Jing, J. Zbontar, et al. Implicit rank-minimizing autoencoder. *Advances in Neural Information Processing Systems*, 33:14736–14746, 2020.
- [64] R. T. Q. Chen, Y. Rubanova, J. Bettencourt, and D. Duvenaud. Neural ordinary differential equations. *arXiv:1806.07366*, 2019.
- [65] Gabriel Peyré and Marco Cuturi. Computational optimal transport. *Foundations and Trends in Machine Learning*, 11:1–257, 3 2018.
- [66] Giancarlo Benettin, Luigi Galgani, Antonio Giorgilli, and Jean-Marie Strelcyn. Lyapunov characteristic exponents for smooth dynamical systems and for hamiltonian systems; a method for computing all of them. part 2: Numerical application. *Meccanica*, 15:21–30, 3 1980.